Drivers of Residual Estuarine Circulation in Tidally Energetic Estuaries: Straight and Irrotational Channels with Parabolic Cross Section

HANS BURCHARD

Leibniz Institute for Baltic Sea Research Warnemünde, Rostock, Germany

ROBERT D. HETLAND

Department of Oceanography, Texas A&M University, College Station, Texas

ELISABETH SCHULZ

Leibniz Institute for Baltic Sea Research Warnemünde, Rostock, Germany

HENK M. SCHUTTELAARS

Delft Institute of Applied Mathematics, Delft University of Technology, Delft, Netherlands

(Manuscript received 19 February 2010, in final form 5 November 2010)

ABSTRACT

The generation of residual circulation in a tidally energetic estuary with constant longitudinal salinity gradient and parabolic cross section is examined by means of a two-dimensional cross-sectional numerical model, neglecting river runoff and Stokes drift. It is shown how the longitudinal and lateral residual circulation can be decomposed into contributions from various processes such as tidal straining circulation, gravitational circulation, advectively driven circulation, and horizontal mixing circulation. The sensitivity of the residual circulation and its components from various processes to changes in forcing is investigated by varying the Simpson number (nondimensional longitudinal buoyancy gradient) and the unsteadiness parameter (nondimensional tidal frequency), as well as the bed roughness and the width of the estuary. For relatively weak salinity gradient forcing, the tidal straining circulation dominates the residual exchange circulation in support of classical estuarine circulation (up-estuary flow near the bed and down-estuary flow near the surface). The strength of the longitudinal estuarine circulation clearly increases with increased salinity gradient forcing. However, when the Simpson number exceeds 0.15, the relative contributions of both gravitational circulation and advectively driven circulation to estuarine circulation increase substantially. Lateral residual circulation is relatively weak for small Simpson numbers and becomes flood oriented (divergent flow near the bed and convergent flow near the surface) for larger Simpson numbers because of increasing contributions from gravitational and advectively driven circulation. Increasing the unsteadiness number leads to decreased longitudinal and lateral residual circulation. Although changes in bed roughness result in relatively small changes in residual circulation, results are sensitive to the width of the estuary, mainly because of changes in residual exchange circulation driven by tidal straining.

1. Introduction

The aim of this study is to quantify the contributions of major processes to longitudinal and lateral residual circulation in tidally energetic estuaries. For this purpose, a two-dimensional cross-sectional numerical model is applied, with prescribed longitudinal salinity gradients and barotropic pressure gradients induced by semidiurnal tidal forcing, under the assumption that all other longitudinal gradients are negligible. The residual circulation is decomposed into residual exchange and local runoff contributions from straining, gravitational circulation, lateral advection, and lateral mixing, both in the longitudinal and lateral directions. Zero net river discharge and a rigid lid (neglect of Stokes drift) are

Corresponding author address: Hans Burchard, Leibniz Institute for Baltic Sea Research Warnemünde, Seestraße 15, D-18119 Rostock, Germany.
E-mail: hans.burchard@io-warnemuende.de

assumed, and a symmetric, parabolic bathymetry is used. Effects of the earth's rotation, wind straining, bathymetric variations, residual river runoff, and Stokes drift will be investigated in follow-up studies. The major tool used in the present study is the estuarine circulation analysis recently introduced by Burchard and Hetland (2010). This analysis provides a semianalytical decomposition of the residual flow profiles into contributions from all processes included in the momentum balance. These contributions are solved numerically, because analytical solutions are available only for strongly simplified situations. This analysis tool is extended here for two-dimensional cross-sectional models, including longitudinal, lateral, and vertical velocity components.

This semianalytical method is based on the same principles as previous approaches that applied a vertically and temporally constant eddy viscosity and calculated contributions to residual currents by tidally averaging the momentum equations and vertically integrating the resulting equations twice (Hansen and Rattray 1965; Chatwin 1976; MacCready 2004; Huijts et al. 2006). Recently, Huijts et al. (2009) demonstrated how analytical solutions for the major contributions to residual currents can be obtained for longitudinal and lateral components, assuming constant eddy viscosity (thus eliminating tidal straining) and diagnostically prescribed lateral density gradients (thus removing parts of the contributions from lateral advection driven by lateral density gradients). In the present study, some simplifications made by Huijts et al. (2009) due to the requirement for analytical solutions are removed by solving the resulting complex analytical expressions numerically. Apart from that, we follow the approach of Huijts et al. (2009).

Classically, estuarine circulation has been attributed to gravitational circulation (see Pritchard 1952, 1954, 1956; Hansen and Rattray 1965; Chatwin 1976). The analytical solutions for gravitational circulation based on constant eddy viscosity originally presented by Hansen and Rattray (1965) have been extended to include wind straining (Wong 1994; Ralston et al. 2008) and parabolic eddy viscosity (McGregor 1972; Ianniello 1977; Burchard and Hetland 2010). All these theories have in common that a tidal modulation of the estuarine circulation other than a modification of the tidal-mean eddy viscosity is not considered.

Effects of ebb–flood asymmetries in vertical differential advection have first been acknowledged by van Aken (1986) and Simpson et al. (1990) as processes leading to a destabilization of the water column during flood (denser offshore waters sheared over less dense onshore waters) and vice versa during ebb. Jay and Musiak (1994) suggested a mechanism how the associated tidal mixing asymmetry (enhancement of vertical mixing during flood and suppression of vertical mixing during ebb) contributes to estuarine circulation: during flood, considerably more momentum is mixed down to the near-bottom region than during ebb, resulting in a near-bottom up-estuary excess velocity. In the present study, this contribution to estuarine circulation is referred to as tidal straining circulation. Burchard and Baumert (1998) showed in a (two-dimensional longitudinal) numerical model study of a partially mixed estuary that this tidal straining circulation contributes more to the generation of estuarine circulation than gravitational circulation. The importance of tidal straining circulation has later been highlighted by Stacey et al. (2001, 2008). Recently, Burchard and Hetland (2010) showed for periodically mixed estuaries that the tidal straining amounts to typically two-thirds of the estuarine circulation (with a one-third contribution from gravitational circulation) for negligible wind stress, no river discharge, and no effects from the earth's rotation and channel geometry. However, this dominance of the tidal straining was shown to decrease with the stability of the flow.

Another important mechanism for creating estuarine circulation has been proposed by Lerczak and Geyer (2004), who found in an idealized model study of a straight channelized estuary that redistribution of longitudinal momentum by lateral advection generates residual currents in support of estuarine circulation. The underlying mechanism for generating the lateral circulation required for this advectively driven redistribution has already been described by Nunes and Simpson (1985) for weakly stratified estuaries: during flood, lateral differential advection builds up a salinity maximum in the center line of the estuary, which leads to lateral salinity gradients toward both sides of the estuary, generating in turn a lateral estuarine circulation with near-bottom currents directed to the sides and converging near-surface currents, both associated with downwelling in the center of the flow. With this, the advectively driven contribution to estuarine circulation can be explained as follows: During flood, the higher longitudinal momentum is advected near the bottom toward the sides (there increasing momentum). Furthermore, the downwelling advects faster near-surface currents down to the near-bottom region in the center of the flow. As a compensation, near the surface, slower velocities are advected toward the center of the flow, there decreasing the flood momentum. Because the same happens during ebb, but with different signs of velocities and their gradients (such that the advective terms have the same sign during ebb and flood), a residual current with a near-bottom up-estuary component is forced. This mechanism has recently been confirmed for stratified

estuaries by means of idealized (Cheng and Valle-Levinson 2009) and realistic numerical model simulations (Scully et al. 2009; Cheng et al. 2009). For scenarios with weak stratification, Lerczak and Geyer (2004) found that this advectively driven contribution to estuarine circulation is of the same order of magnitude as the gravitational circulation. Moreover, the advectively driven contribution to residual longitudinal circulation scales roughly with the relative longitudinal buoyancy gradient (Scully et al. 2009), as well as the gravitational circulation (Geyer et al. 2000) and the tidal straining circulation (Burchard and Hetland 2010).

For one-dimensional geometries, Burchard and Hetland (2010) had identified the covariance between longitudinal vertical shear and eddy viscosity as the tidal straining contribution to estuarine circulation, as sketched by Jay and Musiak (1994). In the more complex two-dimensional situation investigated here, the modification of longitudinal shear by lateral advection additionally impacts on this shear–viscosity covariance, such that it cannot be identified with classical longitudinal straining alone anymore. In the present theory, it will not be possible to differentiate between the impacts of these two effects on the shear–viscosity covariance. Therefore, we are using the term "tidal straining" here in a more general sense, including all contributions to the shear–viscosity covariance.

In the present study, we focus on the quantification of these three processes (tidal straining, gravitational, and advectively driven circulations) and their lateral variation in such a way that the superposition of these contributions exactly amounts to the estuarine circulation. By doing so, a complete decomposition of the lateral, longitudinal, and vertical components of the estuarine circulation into its contributions from these processes is obtained. The parameter space under consideration covers variations in the relative longitudinal buoyancy gradient (Simpson number) and the relative tidal frequency (unsteadiness parameter). Furthermore, the sensitivity of the composition of estuarine circulation on bed roughness and the width of the estuary is tested.

The use of a constant in time and space longitudinal salinity gradient restricts this study to periodically mixed estuaries, of which a few examples exist (Burchard and Hetland 2010). However, by going toward the limit of almost permanently stratified estuaries, it is shown here how the dynamical regime shifts from tidal straining dominated to gravitationally and advectively dominated, as it is assumed for partially mixed estuaries.

This manuscript is organized as follows: First, major nondimensional numbers are defined (section 2a) and the underlying dynamic equations are given (section 2b). In section 2c, the residual circulation analysis is outlined (see the appendix for details). The numerical model is briefly described in section 3. Various scenarios are discussed in detail in section 4, with emphasis on a reference scenario (section 4a), the dependence on the Simpson number (section 4b), the unsteadiness parameter (section 4c), the bed roughness (section 4d), and the channel width (section 4e). Some conclusions are given in section 5.

2. Theory

a. Nondimensional numbers

Two dimensionless numbers have been shown to determine the basic dynamics in nonrotational tidal estuaries with relatively small tidal range: the Simpson number (Simpson et al. 1990; Monismith et al. 1996; Stacey et al. 2001),

$$Si = \frac{\partial_x b H^2}{U_*^2}, \qquad (1)$$

and the "unsteadiness parameter" (Ianniello 1977; Baumert and Radach 1992; Burchard 2009),

$$Un = \frac{\omega H}{U_*}. \qquad (2)$$

Here, $\partial_x b$ is the tidally averaged longitudinal buoyancy gradient, H is the reference (e.g., the mean) water depth, U_* is a scale for the bottom friction velocity, and $\omega = 2\pi/T$ is the tidal frequency with the tidal period T. The Simpson number can be interpreted as the relative buoyancy gradient, and the unsteadiness number can be interpreted as the relative tidal frequency.

It should be noted that, in earlier papers (Monismith et al. 1996; Stacey et al. 2001; Burchard 2009), the Simpson number defined in (1) has generally been denoted as the horizontal Richardson number. However, to acknowledge the introduction of this number by Simpson et al. [1990, see their Eq. (5)], the notation Simpson number is introduced here. The unsteadiness parameter defined in (2) has been denoted in earlier papers (Baumert and Radach 1992; Burchard 2009) as the inverse Strouhal number, but here we suggest using the term unsteadiness parameter to avoid suggesting a relation to eddy shedding processes, which are generally associated with a Strouhal number.

In the field, it is much easier to measure a velocity scale that is directly related to a current velocity rather than to a friction velocity. Furthermore, in numerical modeling, tidal velocity amplitudes are much more the external control parameters than friction velocities. However, from a theoretical point of view, the friction
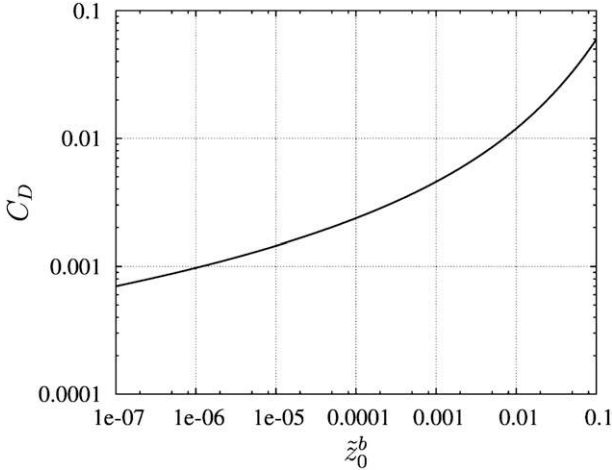
FIG. 1. Conversion factor C_D between friction velocity squared U_*^2 and vertically averaged velocity squared U_t^2 as function of the nondimensional roughness length $\tilde{z}_0^b = z_0^b/H$.

FIG. 2. Sketch of the orientation of the coordinate system and the velocity components with respect to the cross-sectional model domain.

velocity need to be used in the dimensionless parameters Si and Un to emphasize effects of mixing. A useful conversion between friction velocity scale U_* and current velocity scale U_t can be obtained by assuming a logarithmic velocity profile at maximum current speed with a bulk drag coefficient

$$C_D = \left(\frac{U_*}{U_t}\right)^2 = \left\{\frac{\kappa}{\left(1 + \frac{z_0^b}{H}\right)\ln\left(\frac{\overline{H}}{z_0^b} + 1\right) - 1}\right\}^2, \quad (3)$$

with the average water depth $\overline{H}$ and the van Karman number $\kappa = 0.4$. In this context, the nondimensional bottom roughness length, $\tilde{z}_0^b = z_0^b/\overline{H}$, is the only variable determining this conversion (see Fig. 1). It should be noted that (3) provides a conversion between two useful scales, which is mathematically only correct for a logarithmic velocity profile extending throughout the water column. For strongly stratified water columns, C_D will also depend on the stratification.

b. Dynamical equations

Assuming an infinitely long straight estuary of uniform cross-sectional bathymetry, driven by a constant longitudinal buoyancy gradient $[\partial_x b]$, and a periodically varying longitudinal barotropic pressure gradient function $[P^x](t)$, constant in space, the hydrostatic dynamic equations along and across the estuary can be written as (note that diagnostic variables are set in square brackets)

$$\partial_t u + \partial_y(uv) + \partial_z(uw) - \partial_z(A_v\partial_z u) - \partial_s(A_s\partial_s u) - fv$$

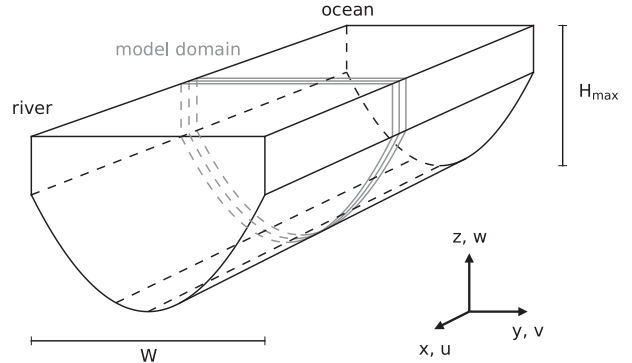$$= \int_z^0 [\partial_x b]\, d\bar{z} - [P^x](t) \quad \text{and} \quad (4a)$$

$$\partial_t v + \partial_y(vv) + \partial_z(vw) - \partial_z(A_v\partial_z v) - \partial_s(A_s\partial_s v) + fu$$

$$= \int_z^0 \partial_y b\, d\bar{z} - P^y(y,t), \quad (4b)$$

with the longitudinal velocity component $u(y, z, t)$, the lateral velocity component $v(y, z, t)$, and the vertical velocity component $w(y, z, t)$ (see Fig. 2 for the orientation of the model domain). Here, $A_v(y, z, t)$ is the vertical eddy viscosity and A_s is the constant mixing coefficient along the σ-coordinate layers with $\sigma(y, z) = \{H(y) + z\}/H(y) - 1$. The term f is the Coriolis parameter, which is included in the equations and subsequent mathematical reformulations for future reference only. The buoyancy $b(y, z, t) = -g\{\rho(y, z, t) - \rho_0\}/\rho_0$ [with density $\rho(y, z, t)$ and reference density $\rho_0 = 1000$ kg m^{-3}] is here calculated by means of a linear equation of state,

$$b = -g\beta S, \quad (5)$$

with the haline contractivity β for which we choose the constant value $\beta = 7.8 \times 10^{-4}$ psu^{-1}. The flow is assumed to be nondivergent in the y–z plane,

$$\partial_y v + \partial_z w = 0. \quad (6)$$

The longitudinal barotropic pressure gradient function $[P^x](t)$ is calculated such that

$$Q(t) = \int_A u(y, z, t)\, dA = Q_0 + Q_t \cos(\omega t)$$

$$= A\left\{U_0 + U_t \cos\left(2\pi\frac{t}{T}\right)\right\}, \quad (7)$$

with the constant cross-sectional area $A = \int_0^W H(y)\, dy$, the residual and tidal cross-sectional volume transports Q_0 and Q_t, the residual and the tidal cross-sectionally averaged velocities U_0 and U_t, and the width of the

estuary W. Note that Q_0 and U_0 are set to zero in the present study. The cross-sectionally averaged tidal velocity amplitude U_t is the velocity scale used to calculate the friction velocity scale U_* [see (3)]. The lateral pressure gradient function $P^y(y, t)$ is calculated such that

$$\int_{-H(y)}^0 v(y, z, t)\, dz = 0: \tag{8}$$

that is, such that the depth-mean lateral velocity vanishes and thus the surface elevation is kept at its initial state $\eta(y, t) = 0$. By doing so, a rigid-lid condition is obtained (see also Huijts et al. 2009), an approximation which substantially simplifies the analysis here. With this, the Stokes drift as process generating subtidal flows is excluded, an effect that is, for long estuaries with tidal waves propagating up estuary, generally counteracting the subtidal flows driven by buoyancy effects (Li et al. 1998; Li and O'Donnell 2005). The salinity is calculated by means of the following budget equation:

$$\partial_t S + u[\partial_x S] + v\partial_y S + w\partial_z S - \partial_z(K_v\partial_z S) - \partial_s(A_s\partial_s S) = 0, \tag{9}$$

where K_v is the eddy diffusivity. The longitudinal salinity gradient $\partial_x S$ is prescribed in such a way that it is consistent with the prescribed buoyancy gradient $\partial_x b$ in the sense that the equation of state, (5), is fulfilled. The longitudinal salinity gradient will be kept at a value constant in time and space in all scenarios considered here. However, it is well known that, for high Simpson numbers, this would lead to a runaway stratification with negative salinities, preventing periodic solutions (Blaise and Deleersnijder 2008). In real estuaries, there is a feedback from the salinity to the horizontal salinity gradient, in the sense that the gradient has a maximum in the center of the salt wedge and converges to zero toward maximum and minimum salinity values.

Dynamic boundary conditions are assuming law of the wall dynamics near the bottom and a prescribed turbulent momentum flux (τ_x^s, τ_y^s) at the surface the direction of which is opposed to the near-surface wind direction. Note that the surface momentum flux is considered in the derivations here for future reference only. Buoyancy fluxes are assumed to be zero across all boundaries.

The eddy viscosity A_v and the eddy diffusivity K_v are calculated by means of a turbulence closure model (see section 3).

c. Residual circulation analysis

As shown in the appendix, the dynamic equations in (4) for u and v can be analytically transformed in such a way that mathematical expressions for the tidally averaged velocity profiles $\langle u \rangle$ and $\langle v \rangle$ are obtained,

$$\langle u \rangle = \sum_{i=1}^6 \langle u_i^e \rangle + \gamma(y, z)U_r(y) \quad \text{and} \tag{10a}$$

$$\langle v \rangle = \sum_{i=1}^6 \langle v_i^e \rangle, \tag{10b}$$

with the nondimensional local runoff function $\gamma(y, z)$, the vertical average of which is unity everywhere, and the vertical-mean local runoff, $U_r(y) = \int_{-H(y)}^0 \langle u \rangle(y, z)\, dz$. The longitudinal residual velocity component in (10a) is presented as the sum of seven velocity profiles, of which the first six are exchange profiles with zero vertical mean, and the last one is the local runoff profile. The lateral velocity profiles are also decomposed into six exchange profiles with zero vertical mean, but without a contribution from a nonzero runoff profile. All velocity profiles have zero bottom velocity, which is consistent with the no-slip bottom boundary condition. In a similar way as in Burchard and Hetland (2010), the six residual exchange circulation profiles have the following meanings:

1) $\langle u_1^e \rangle$ and $\langle v_1^e \rangle$ are exchange profiles due to the covariance between the eddy viscosity and the longitudinal and the lateral vertical shear, because $\langle A_v'\partial_z u' \rangle$ and $\langle A_v'\partial_z v' \rangle$, of which classical tidal straining (Jay and Musiak 1994) is an important part. Other straining processes, such as the lateral advection of longitudinal shear, may also contribute to this shear–viscosity covariance. This term would be zero for an eddy viscosity constant in time, as assumed in the classical theory of Hansen and Rattray (1965).

2) $\langle u_2^e \rangle$ and $\langle v_2^e \rangle$ are exchange profiles due to gravitational acceleration, because these are the only terms containing the longitudinal and the lateral buoyancy gradients. Therefore, these terms can be denoted as the gravitational circulation profiles.

3) $\langle u_3^e \rangle$ and $\langle v_3^e \rangle$ are exchange profiles due to surface stresses and can therefore be denoted as the wind straining circulation terms.

4) $\langle u_4^e \rangle$ and $\langle v_4^e \rangle$ are exchange profiles due to lateral and vertical advection and will therefore be denoted as advectively driven residual circulation profiles. Contributions from horizontal and vertical advection are combined here to present advection along sloping coordinates (such as the bottom) as one process.

5) $\langle u_5^e \rangle$ and $\langle v_5^e \rangle$ are exchange profiles due to lateral (along coordinate) mixing, a process parameterizing eddy-related lateral transport of momentum caused by processes not resolved in a two-dimensional lateral model such as lateral shear instabilities.

6) $\langle u_6^e \rangle$ and $\langle v_6^e \rangle$ are exchange profiles due to the Coriolis rotation.

The longitudinal residual flow profile $\langle u \rangle$ can also be formulated in another way,

$$\langle u \rangle = \sum_{i=1}^{6} \langle u_i^a \rangle \qquad (11)$$

(see the appendix). By doing so, the residual local runoff contribution in (10a), γU_r, is distributed to the individual total (exchange + local runoff) contributions $\langle u_i^a \rangle$ (see Huijts et al. 2009). This alternative way of calculating contributions to residual circulation will be compared to the residual exchange circulation profiles $\langle u_i^e \rangle$. The latter focuses on vertical exchange in estuaries, whereas the former quantifies the contributions of various processes on lateral and vertical exchange.

3. Numerical model

As a numerical modeling tool, the General Estuarine Transport Model (GETM; see online at http://www.getm.eu and see Burchard and Bolding 2002) has been used in a two-dimensional vertical mode covering the cross-sectional y–z plane. Such lateral GETM scenarios have already been applied by Umlauf et al. (2010) for studying channelized dense bottom currents and by Hofmeister et al. (2010) to quantify numerical mixing in a coastal upwelling scenario. Both horizontal velocity components are calculated such that the interaction between longitudinal and lateral components through advection and Coriolis rotation can be included. The advantage of this two-dimensional approach over a full three-dimensional model with approximately homogeneous conditions in the longitudinal direction (see, e.g., Lerczak and Geyer 2004; Chen and Sanford 2009; Cheng and Valle-Levinson 2009) is the high spatial resolution at comparably low computational effort. In the lateral model, gradients in the longitudinal direction are either neglected (as for the velocity gradients) or prescribed (as for the salinity gradient). The barotropic forcing is applied in a way that in each time step the longitudinal velocity is corrected by a constant value such that the prescribed transport according to (7) is achieved (see Burchard 1999). The rigid-lid condition is fulfilled by correcting the lateral velocity in each water column by a constant value such that the vertical mean vanishes [see (8)].

As turbulence closure model, a two-equation k–ε model with transport equations for the turbulent kinetic energy (TKE) k and the dissipation rate of the TKE ε is used. These equations are coupled to a second-moment closure suggested by Cheng et al. (2002). Details of the closure model are given by Umlauf and Burchard (2005) and Burchard and Hetland (2010). This type of closure model has proven to quantitatively reproduce marine and limnic turbulence observations (see, e.g., Simpson et al. 2002; Burchard et al. 2002; Stips et al. 2002; Arneborg et al. 2007).

To minimize numerical dissipation and mixing, the advection terms for momentum and salinity are calculated by means of nonlinear monotone [total variation diminishing (TVD)] one-dimensional methods in a directional split mode. The scheme used here is a third-order monotone Universal Limiter for Transport Interpolation Modeling of the Advective Transport Equation Quadratic Upstream Interpolation for Convective Kinematics with Estimated Upstream Terms (ULTIMATE QUICKEST) method (see Leonard 1991; Pietrzak 1998; for numerical tests, see Burchard and Bolding 2002).

As the lateral depth distribution, a symmetric parabolic function has been chosen, with a maximum depth of $H_{\max} = 15$ m in the center and a minimum depth of $H_{\min} = 5$ m at the sides (see Fig. 2) as in Lerczak and Geyer (2004). Thus, the average depth is $\overline{H} = 11.67$ m. The width of the estuary is $W = 1000$ for most cases, except for the study of sensitivity to width, where $W = 500$ m and $W = 2000$ m are used. With changed estuary width, the tidal volume flux Q_t had to be adjusted to give the correct cross-sectionally averaged tidal velocity U_t. For all scenarios, the lateral mixing coefficient for momentum and salinity is set to a constant value of $A_s = 1$ m^2 s^{-1}. All simulations are executed for 10 tidal periods, with the M_2 period of $T = 44\ 714$ s. Only the 10th period is analyzed here, at which a periodic state is reached to high accuracy for all scenarios. The numerical resolution is high, with 100 σ layers in the vertical with strong zooming toward the bed, where the bottom grid box in the deepest point has a thickness of 0.02 m. Only for strong stratification (Si > 0.18) 150 layers with additional zooming toward the surface are used. The horizontal resolution is generally $\Delta y = 5$ m, only in the case of $W = 2000$ m a horizontal resolution of $\Delta y = 10$ m is used. The time step for most simulations is $\Delta t = T/20\ 000 \approx 2.2$ s, except for scenarios with Si > 0.18, where $\Delta t = T/40\ 000 \approx 1.1$ s had to be used to obtain numerical stability.

The residual circulation analysis is carried out inside the numerical model, averaging the relevant terms using all time steps during the last of 10 tidal periods. To calculate A'_v, u', and v' during each time step of the 10th tidal period, the tidal-mean values $\langle A_v \rangle$, $\langle u \rangle$, and $\langle v \rangle$ are calculated already during the 9th tidal period.

The momentum advection terms are calculated exactly as they occur in the discretized momentum equations, using the TVD alternating direction schemes presented

TABLE 1. Specifications of the scenarios simulated for the present study. Scenario 01 is the reference scenario in relation to which external parameters have been changed for the other scenarios (marked in italics).

No.	Scenario	U_t (m s^{-1})	U_* (m s^{-1})	$\partial_x S$ (psu m^{-1})	z_0^b (m)	W (m)	Si	Un
01	Reference	1.0	4.78×10^{-2}	-2.0×10^{-4}	10^{-3}	1000	9.11×10^{-2}	3.43×10^{-2}
02	Small Si	1.0	4.78×10^{-2}	-1.0×10^{-4}	10^{-3}	1000	4.56×10^{-2}	3.43×10^{-2}
03	Large Si	1.0	4.78×10^{-2}	-4.0×10^{-4}	10^{-3}	1000	1.82×10^{-1}	3.43×10^{-2}
04	Small Un	2.0	9.56×10^{-2}	-8.0×10^{-4}	10^{-3}	1000	9.11×10^{-2}	1.71×10^{-2}
05	Large Un	0.5	2.39×10^{-2}	-5.0×10^{-5}	10^{-3}	1000	9.11×10^{-2}	6.86×10^{-2}
06	Small z_0^b	1.28	4.78×10^{-2}	-2.0×10^{-4}	10^{-4}	1000	9.11×10^{-2}	3.43×10^{-2}
07	Large z_0^b	0.73	4.78×10^{-2}	-2.0×10^{-4}	10^{-2}	1000	9.11×10^{-2}	3.43×10^{-2}
08	Small W	1.0	4.78×10^{-2}	-2.0×10^{-4}	10^{-3}	500	9.11×10^{-2}	3.43×10^{-2}
09	Large W	1.0	4.78×10^{-2}	-2.0×10^{-4}	10^{-3}	2000	9.11×10^{-2}	3.43×10^{-2}

in section 3, without direct rediscretization. This procedure reduces the discretization error of the residual circulation analysis.

4. Scenario studies

A reference scenario and a number of sensitivity scenarios with variation of the Simpson number Si, the unsteadiness parameter Un, the bed roughness length z_0^b, and the width of the estuary W are discussed here.

Practically, the cross-sectionally averaged velocity amplitude U_t and the longitudinal salinity gradient $\partial_x S$ are prescribed. Furthermore, the bed roughness and the bathymetry [including the depth $H(y)$ and the width W] are directly prescribed, as well as the tidal frequency $\omega = 2\pi/T$ with $T = 44\ 714$ s.

To obtain a certain combination of target values for Si and Un, Eqs. (1) and (2), using (3) and (5), are solved for U_t and $\partial_x S$,

$$U_t = \frac{\omega \overline{H}}{C_D^{1/2} \text{Un}}, \quad \partial_x S = \frac{-\omega^2 \text{Si}}{g\beta \text{Un}^2}, \qquad (12)$$

where the average depth $\overline{H} = 11.67$ m is used. Here, C_D is calculated from (3). All settings for these scenarios are given in Table 1.

To increase generality, the results for the different scenario calculations are presented as nondimensional quantities. All current velocities are normalized by the tidal velocity amplitude U_t,

$$(\tilde{u}, \tilde{v}, \tilde{w}) = \frac{(u, v, w)}{U_t};$$

$$(\langle \tilde{u}_i^e \rangle, \langle \tilde{v}_i^e \rangle, \langle \tilde{w}_i^e \rangle) = \frac{(\langle u_i^e \rangle, \langle v_i^e \rangle, \langle w_i^e \rangle)}{U_t}; \quad \text{and}$$

$$\langle \tilde{u}_i^a \rangle = \frac{\langle u_i^a \rangle}{U_t}. \qquad (13)$$

All quantities related to mixing are normalized by the friction velocity scale U_* and the average depth $\overline{H}$,

$$\tilde{A}_v = \frac{A_v}{U_* \overline{H}}; \quad \langle \tilde{A}_v \partial_z \tilde{u} \rangle = \frac{\langle A_v \partial_z u \rangle}{U_*^2}; \quad \langle \tilde{A}_v \partial_z \tilde{v} \rangle = \frac{\langle A_v \partial_z v \rangle}{U_*^2}. \qquad (14)$$

To quantify the intensity of exchange flows, typically the rms velocity (Lerczak and Geyer 2004) or the average of the absolute value of the velocity component under consideration is calculated (Burchard and Hetland 2010). However, the disadvantage of these approaches is that the values of the individual contributions do not add up to the total residual. Furthermore, the orientation of the exchange flows (near-bottom currents up estuary or down estuary) is not included. To avoid these disadvantages, we propose here an alternative measure of exchange flow intensity,

$$\mathcal{M}(\langle \tilde{u}_i^e \rangle)$$
$$= -\frac{1}{W} \int_0^W \frac{4}{\{H(y)\}^2} \int_{-H(y)}^0 \langle \tilde{u}_i^e(y, z) \rangle \left\{ z + \frac{H(y)}{2} \right\} dz\, dy. \qquad (15)$$

The expression in the inner integral is motivated by the straining term of the potential energy anomaly equation (van Aken 1986; Burchard and Hofmeister 2008). The expression is scaled here in such a way that, for a step-like exchange flow with a value of $\langle \tilde{u} \rangle = +1$ everywhere below local middepth and a value of $\langle \tilde{u} \rangle = -1$ everywhere above local middepth, a value of $\mathcal{M}(\langle \tilde{u} \rangle) = 1$ is resulting. For exchange flows opposing classical estuarine circulation, $\mathcal{M}(\langle \tilde{u} \rangle)$ will be negative. For pronounced exchange flows, the value of $\mathcal{M}(\langle \tilde{u} \rangle)$ is similar to the cross-sectionally averaged absolute velocity. It should be noted that $\mathcal{M}(\langle \tilde{u} \rangle)$ quantifies only the residual exchange circulation parts of the residual current contributions; that is, for a residual flow with horizontal but without vertical shear, $\mathcal{M}(\langle \tilde{u} \rangle) = 0$ would be obtained. For the case of the residual velocity in the reference scenario, $\mathcal{M}(\langle \tilde{u} \rangle) = 0.0406$, which compares well to the average

TABLE 2. Measure of the nondimensional longitudinal residual exchange flow intensity $\mathcal{M}(\langle \tilde{u} \rangle)$, as defined in (15). Positive values are supporting classical estuarine circulation (near-bottom up-estuary flow), and negative values are opposing it.

No.	Scenario	$\mathcal{M}(\langle \tilde{u} \rangle)$ (residual)	$\mathcal{M}(\langle \tilde{u}_1^e \rangle)$ (strain)	$\mathcal{M}(\langle \tilde{u}_2^e \rangle)$ (gravitational)	$\mathcal{M}(\langle \tilde{u}_4^e \rangle)$ (advectively driven)	$\mathcal{M}(\langle \tilde{u}_5^e \rangle)$ (horizontal mixing)	$\mathcal{M}(\gamma \tilde{U}_r)$ (local)	$\mathcal{M}(\langle \tilde{u}_{err} \rangle)$ (error)
01	Reference	+0.0406	+0.0273	+0.0046	+0.0071	−0.0000	+0.0010	−0.0006
02	Small Si	+0.0203	+0.0148	+0.0018	+0.0032	−0.0000	+0.0003	−0.0002
03	Large Si	+0.0972	−0.0130	+0.0544	+0.0576	−0.0018	−0.0019	−0.0020
04	Small Un	+0.0400	+0.0191	+0.0054	+0.0125	−0.0001	−0.0019	−0.0012
05	Large Un	+0.0140	+0.0096	+0.0033	+0.0008	−0.0000	+0.0001	−0.0002
06	Small z_0^b	+0.0347	+0.0211	+0.0039	+0.0083	−0.0001	+0.0008	−0.0007
07	Large z_0^b	+0.0473	+0.0341	+0.0056	+0.0056	−0.0000	+0.0012	−0.0008
08	Small W	+0.0278	+0.0166	+0.0040	+0.0060	−0.0001	+0.0008	−0.0005
09	Large W	+0.0521	+0.0414	+0.0049	+0.0048	−0.0000	+0.0004	−0.0005

absolute nondimensional residual velocity of 0.0422. For all scenarios, these longitudinal exchange flow intensities are given in Table 2. It can be seen that the intensities of the contributions to the exchange flow add up to the intensity of the exchange flow, up to a small discretization error, which is given as well.

The velocity scale defined in (15) can also be used for the lateral circulation components, assuming lateral symmetry,

$$
\mathcal{M}(\langle \tilde{v}_i^e \rangle) \\
= -\frac{2}{W} \int_{W/2}^{W} \frac{4}{\{H(y)\}^2} \int_{-H(y)}^{0} \langle \tilde{v}_i^e(y,z) \rangle \left\{ z + \frac{H(y)}{2} \right\} dz \, dy,
$$

(16)

with $\mathcal{M}(\langle \tilde{v} \rangle) > 0$ representing a flood-oriented lateral residual circulation (upslope near the bottom).

a. Reference scenario

For the reference scenario, a channel of width $W = 1000$ m with Si = 0.0911 and Un = 0.0343 was chosen. The bed roughness length was set to $z_0^b = 10^{-3}$ m. This results in a classical strain-induced periodic stratification (SIPS; see Simpson et al. 1990) situation with full vertical mixing at the end of the flood and marginally stable stratification during ebb. Figure 3 shows results for velocity and salinity during full flood ($t/T = 0.25$; Figs. 3a,b), slack after flood ($t/T = 0.5$; Figs. 3c,d), full ebb ($t/T = 0.75$; Figs. 3e,f), and slack after ebb ($t/T = 1.0$; Figs. 3g,h). During full flood, salinity is almost vertically homogeneous because of classical flood straining, but, in the center of the channel, salinity is about 0.5 psu higher than at the sides. This is due to longitudinal differential advection of salinity: that is, because the longitudinal velocity has a distinct local maximum in the center of the estuary, where the depth is 3 times as high as at the sides. In turn, the horizontal salinity gradients lead to a weak lateral circulation, with divergent flow at the bed and convergent flow at the surface, as already observed by

Nunes and Simpson (1985) (see also Fig. 4). This lateral circulation is strongly enhanced to a lateral velocity of up to $\tilde{v} = 0.07$ by the end of the flood, when vertical mixing is reduced because of decreasing bed shear such that the dense, saline water masses in the center of the flow sink down. Furthermore, the longitudinal buoyancy gradient acts in such a way that the near-surface longitudinal flow reverses toward ebb already before slack tide, whereas the near-bottom flow is still flood oriented. At full ebb, horizontal differential advection has already generated a salinity minimum near the surface in the center of the channel, and by the end of the ebb also the bottom salinity in the center of the channel has reached a lateral minimum such that high salinities have accumulated near the sides of the estuary. However, the ebb lateral circulation is very weak. By the end of the ebb, when vertical mixing is reducing, the potential energy of this lateral stratification is released in such a way that strong lateral flow convergence (negative values of $\partial_y v$) is generated near the bed (Fig. 4f), causing significant upwelling in the center of the flow (with a maximum vertical velocity of $\tilde{w} = 0.007$) and flow divergence near the surface.

In Fig. 4, the tidal dynamics are shown in high temporal resolution for the center of the flow. The classical tidal straining as sketched by Jay and Musiak (1994) is clearly visible. During flood ($t/T = 0.25$), denser downstream waters are sheared over less dense upstream waters, which results into marginally unstable stratification (surface salinity exceeds bottom salinity by up to 0.03 psu, which is not visible from Fig. 4c), strong vertical mixing, and velocity profiles that are almost homogeneous in the upper half of the water column. During ebb ($t/T = 0.75$), vertical differential advection forces stabilization of the water column, resulting in marginally stable salinity profiles (Fig. 4c), suppressed vertical mixing (Fig. 4d), and velocity profiles that are sheared up to the surface (Fig. 4a). Because of more intense mixing during flood, the vertical momentum flux is larger during flood
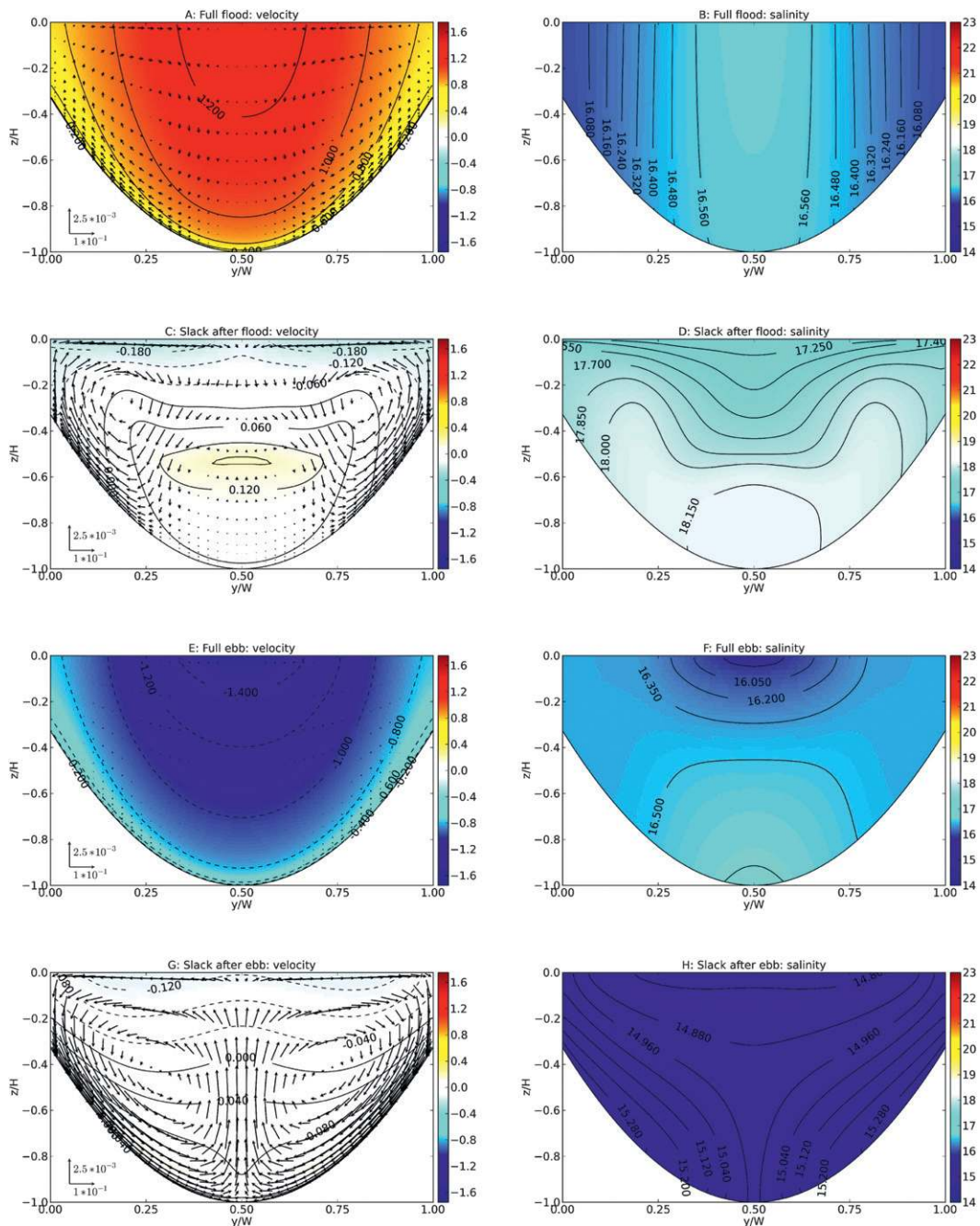
FIG. 3. Scenario 01 (reference) for (a),(b) full flood ($t/T = 0.25$); (c),(d) slack after flood ($t/T = 0.5$); (e),(f) full ebb ($t/T = 0.75$); (g),(h) and slack after ebb ($t/T = 1.0$). (a),(c),(e),(g) Velocity distribution with contours and color scale for longitudinal velocity and arrows for lateral and vertical velocity. The vertical velocity is scaled by the aspect ratio between vertical and horizontal scales. (b),(d),(f),(h) Salinity distribution as contours and color scale.

than during ebb (Fig. 4b). Interestingly, the vertical velocity (Fig. 4e) has maximum values that are shifted in time with respect to the instances of slack tides. The strongest negative vertical velocities after the flood occur at $t/T \approx 0.42$, just when the vertical mixing ceases abruptly (Fig. 4d). The strongest upward velocities occur

at $t/T \approx 0.08$, which coincides with minimum vertical mixing after the ebb current. This asymmetry in transition to low vertical mixing is caused by the fact that the estuarine circulation causes a background shear in the upper part of the water column, which increases ebb shear and decreases flood shear. With this, the phase of active
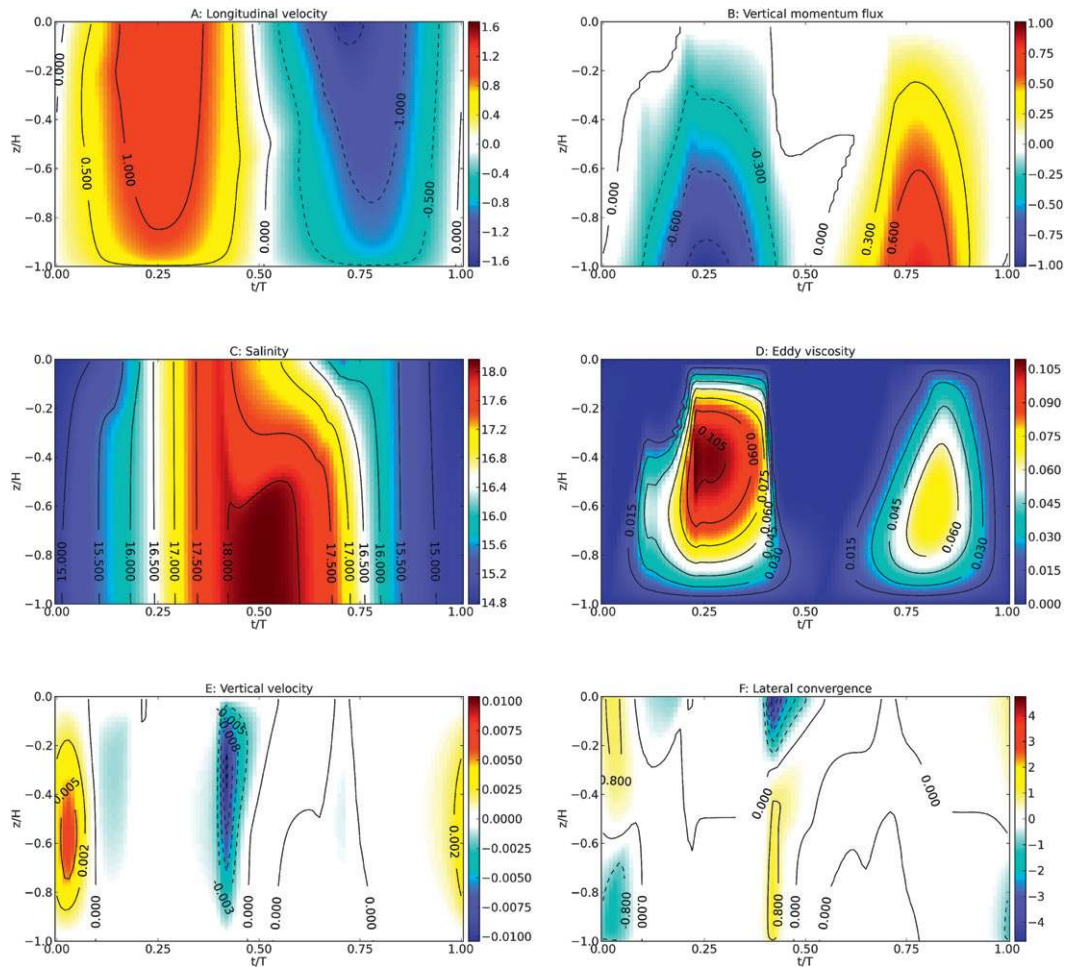
FIG. 4. Scenario 01 (reference): Time series of profiles of (a) longitudinal velocity, (b) vertical momentum flux, (c) salinity, (d) eddy viscosity, (e) vertical velocity, and (f) lateral convergence in the center of the channel.

shear production in the upper half of the water column is significantly shorter during flood than during ebb. It is furthermore clearly seen in Fig. 4f that surface convergence directly coincides with downward vertical velocities in the center of the flow and vice versa.

The tidally resolved dynamics discussed for the reference scenario result in the expected estuarine circulation pattern shown in Fig. 5c. The longitudinal exchange flow pattern shows a remarkable similarity to the flow pattern simulated by Lerczak and Geyer (2004) for their weakly stratified case (their Fig. 8). The residual vertical momentum flux $\langle A_v \partial_z u \rangle$ (Fig. 5d) shows the expected pattern, with negative values in the lower part of the center of the channel because of the observed flood shear dominance in that region.

Figure 6 shows the residual circulation decomposition into major contributions. The left column (Figs. 6a,c,e,g) presents the longitudinal total contributions $\langle \tilde{u}_i^a \rangle$ to the residual circulation according to (11), together adding

up to the residual circulation $\langle \tilde{u} \rangle$. Both the gravitational and the advectively driven component provide strong up-estuary contributions in the center of the flow, compensated by down-estuary contributions near the sides. For the gravitational component, this can be explained such that the baroclinic pressure gradient (forcing up-estuary flow), which increases with depth, is balanced by a depth-independent barotropic pressure gradient (forcing down-estuary flow). Because both have to balance across the estuary, the baroclinic pressure gradient forcing dominates in deeper water and the barotropic pressure gradient dominates in shallower water.

The contribution from the advectively driven total residual circulation $\langle \tilde{u}_4^a \rangle$ is even stronger (see Fig. 6e). During flood, the negative vertical velocity advects positive momentum downward in the center of the channel (Fig. 3a); during ebb, the opposite happens in the center of the channel. Near the sides, momentum advection leads to decrease of longitudinal momentum, both during
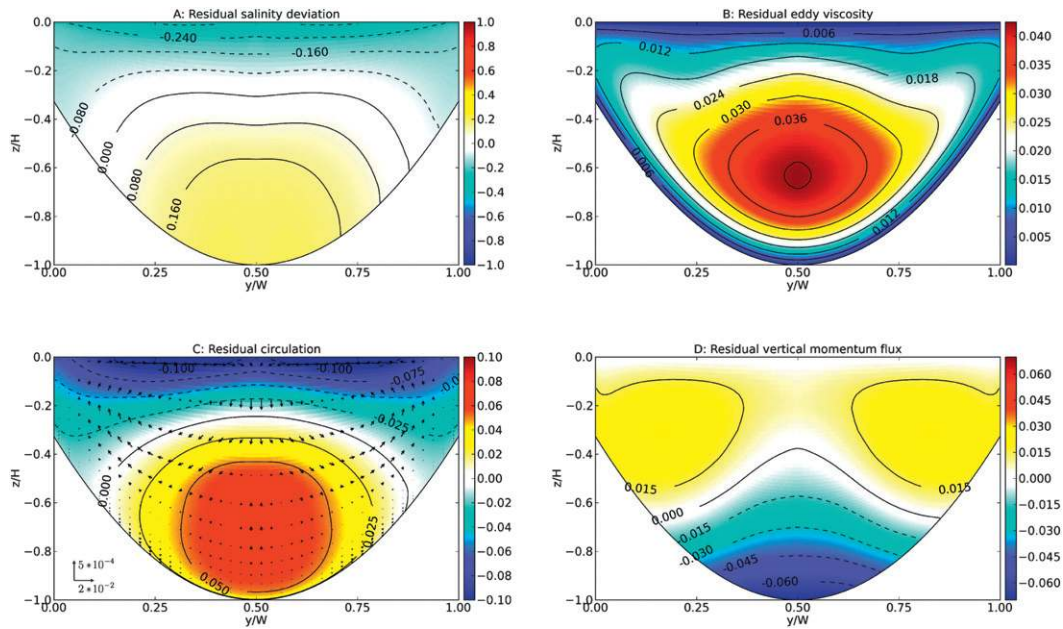
FIG. 5. Scenario 01 (reference): Nondimensional tidal residual results. Velocities are nondimensionalized with the tidal velocity amplitude U_t, and vertical momentum flux and eddy viscosity are nondimensionalized with the friction velocity amplitude U_* and the average depth $\overline{H}$. Vertical velocity components are scaled by the aspect ratio between vertical and horizontal scales: (a) salinity; (b) eddy viscosity; (c) residual velocity ($\langle u \rangle$, $\langle v \rangle$, $\langle w \rangle$); and (d) residual vertical momentum flux, $-\langle A_v \partial_z u \rangle$. The external parameters of the scenario are given in Table 1.

flood and ebb. The contribution from horizontal mixing is opposite to the advectively driven forcing: high positive momentum during flood is decreased in the center of the channel by horizontal mixing and vice versa during ebb.

The total straining contribution to the residual currents is predominantly promoting an estuarine circulation exchange flow in the vertical (Fig. 6a). Additionally, in the lateral direction, up-estuary flows dominate at the sides and down-estuary flow in the center of the channel, thus opposing the lateral contributions from gravitational and advectively driven circulation. Assuming that the total contribution from straining results from a tidal-mean area-integrated balance between vertical momentum flux near the bed (which is negative in the center of the channel and positive at the sides; see Fig. 3d) divided by the local water depth and the negative tidal-mean pressure gradient, it is clear that vertically integrated total straining circulation is down estuary in the center and up estuary at the sides. This can be verified by checking that the tidal-mean vertical momentum flux at the bed, divided by the local depth, vanishes when averaged across the width of the estuary (see Fig. 3d).

The right column of Fig. 6 shows a decomposition of the longitudinal residual velocity $\langle \tilde{u} \rangle$ into residual exchange circulation profiles (Figs. 6b,d,f) and local residual runoff (Fig. 6h) according to (10a). Furthermore,

Table 2 gives quantitative measures for the intensities of the exchange flows $\mathcal{M}(\langle \tilde{u} \rangle)$ [see (15) for the definition]. The intensity of the residual circulation in this case is $\mathcal{M}(\langle \tilde{u} \rangle) = 0.0406$. Clearly, tidal straining [Fig. 6b; $\mathcal{M}(\langle \tilde{u}_1^e \rangle) = 0.0273$], gravitational circulation [Fig. 6d; $\mathcal{M}(\langle \tilde{u}_2^e \rangle) = 0.0046$], and advectively driven circulation [Fig. 6f; $\mathcal{M}(\langle \tilde{u}_4^e \rangle) = 0.0071$] all support classical estuarine circulation, whereas the contribution from horizontal mixing residual exchange circulation [not shown; $\mathcal{M}(\langle \tilde{u}_4^e \rangle) = -0.00004$] is weak. The strongest exchange circulation contribution is thus from tidal straining. The fact that the contributions from gravitational circulation and lateral advection are of the same order of magnitude is in agreement with the findings by Lerczak and Geyer (2004) and Scully et al. (2009). The role of the tidal straining contribution for this parameter combination (relatively weak stratification) is even stronger than shown by Burchard and Hetland (2010) for a one-dimensional geometry. This could be explained by the fact that for flows with lateral variation lateral advection of longitudinal shear additionally contributes to tidal straining.

The up-estuary residual current in the lower half of the center of the flow is furthermore enhanced by a local residual runoff circulation (Fig. 6h), which has a pronounced maximum in the center of the channel. In real, long estuaries with variable water depth and tidal waves
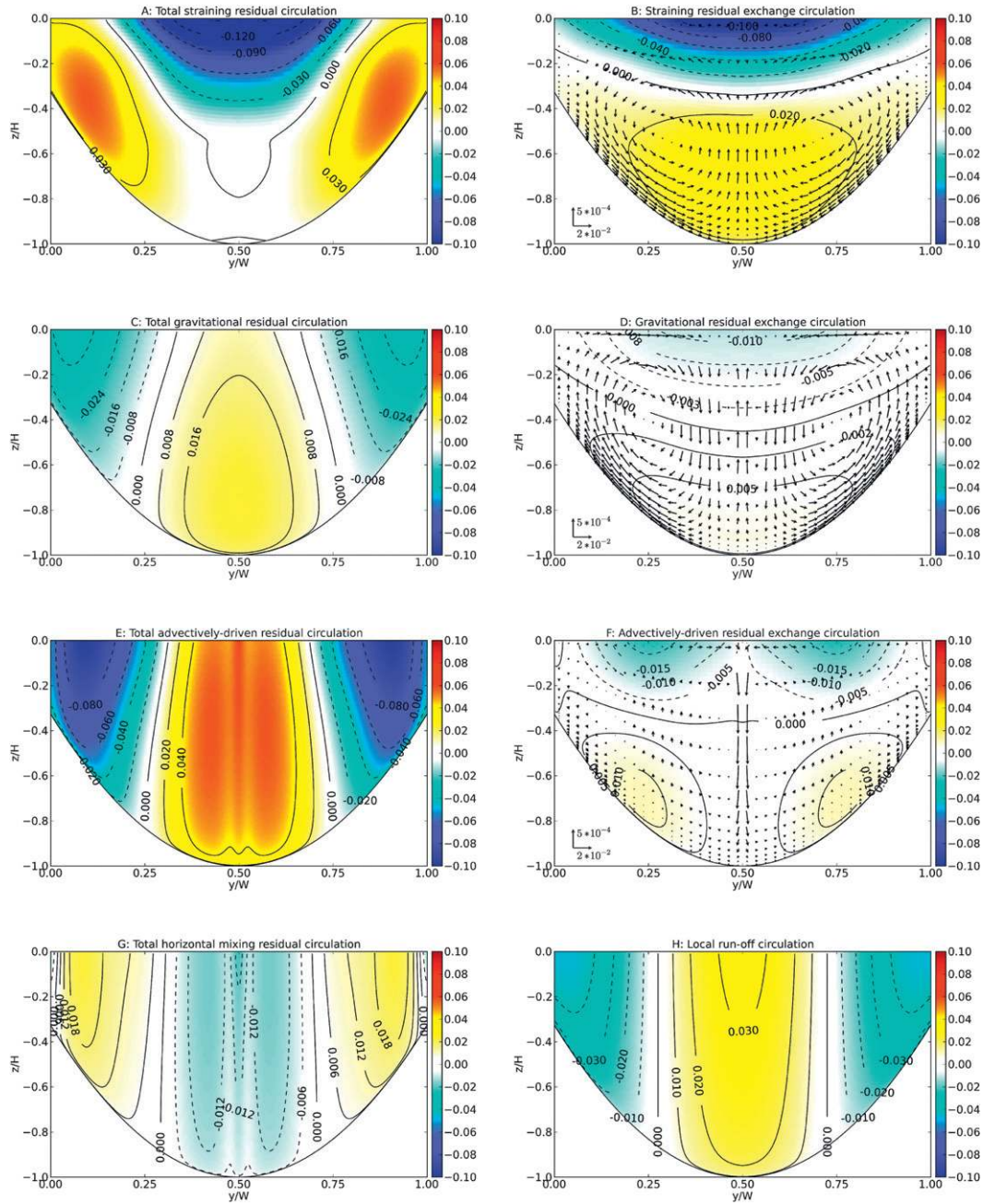
FIG. 6. Scenario 01 (reference): Nondimensional tidal residual velocity profiles. Velocities are nondimensionalized with the tidal velocity amplitude U_t. Vertical velocity components are scaled by the aspect ratio between vertical and horizontal scales. The profiles show (left) total and (right) exchange residual longitudinal velocity contributions: (a) total straining residual circulation $\langle u_1^a \rangle$; (c) total gravitational residual circulation $\langle u_2^a \rangle$; (e) total advectively driven residual circulation $\langle u_4^a \rangle$; (g) total horizontal mixing residual circulation, $\langle u_5^a \rangle$; (b) baroclinic straining residual circulation, $(\langle u_1^e \rangle, \langle v_1^e \rangle, \langle w_1^e \rangle)$; (d) baroclinic gravitational residual circulation $(\langle u_2^e \rangle, \langle v_2^e \rangle, \langle w_2^e \rangle)$; (f) baroclinic advectively driven residual circulation $(\langle u_4^e \rangle, \langle v_4^e \rangle, \langle w_4^e \rangle)$; and (h) residual runoff circulation γU_r. For simplicity, lateral circulation is shown only in the residual exchange circulation panels. The external parameters of this scenario 01 are given in Table 1.

progressing up estuary, the Stokes drift (higher water levels during flood than during ebb) and river discharge would counteract against this longitudinal exchange flow (Li et al. 1998; Li and O'Donnell 2005).

For the central water column, Fig. 7 shows in detail all contributions to the longitudinal residual profile: from the total (exchange + local runoff) residual profiles (Fig. 7a) calculated according to (11), the residual exchange circulation profiles (Fig. 7b) calculated according to (10a), and the local runoff contributions (Fig. 7c) calculated according to the difference between (10a) and (11). The total residual profiles due to straining, gravitation, advection, and horizontal mixing are exactly the sum of the respective exchange and local runoff contributions. In all three panels, the black curve (residual in Figs. 7a,b and local residual in Fig. 7c) is the sum of all the other curves displayed. Figure 7b shows that the residual exchange circulation comes largely from the straining contribution, although its total contribution has almost no up-estuary component (Fig. 7a) because of the down-estuary straining contribution to the local runoff profile (Fig. 7c). The local runoff contributions as well as the local residual runoff profile show shapes like classical logarithmic velocity profiles. Contributions from advection and horizontal mixing residual exchange circulation are negligible in the center of the flow. The former, however, shows two pronounced contributions to estuarine circulation at $y/W = 0.25$ and $y/W = 0.75$ (see Fig. 6). This is in agreement with the study by Lerczak and Geyer (2004) (see also the discussion in section 1). The horizontal mixing residual exchange contribution to estuarine circulation is small throughout the cross section for all scenarios tested (see Table 2). In the following, we emphasize on the analysis of longitudinal and lateral residual exchange circulation, $\langle \tilde{u}_i^e \rangle$ and $\langle \tilde{v}_i^e \rangle$.

The lateral residual circulation is fairly weak for the reference scenario (see Fig. 5c). Near the surface, a two-cell circulation with surface convergence is detectable (consistent with stronger lateral circulation during flood than during ebb), and, near the bed, two cells with weak bottom convergence and positive vertical velocity in the center of the flow can be seen, as characteristic for ebb flow.

Lateral gravitational circulation (Fig. 6d) is directly related to the mean salinity distribution (Fig. 5a) and shows the strongest contribution to lateral residual circulation. Near the bottom, these gravitational currents are directed upslope, driven by the pronounced lateral salinity gradients. Lateral straining circulation is largely opposite to the gravitational circulation, with significant near-bed downslope currents. However, it will be seen that this feature is not persistent throughout most of the sensitivity studies, because small changes in Si and Un
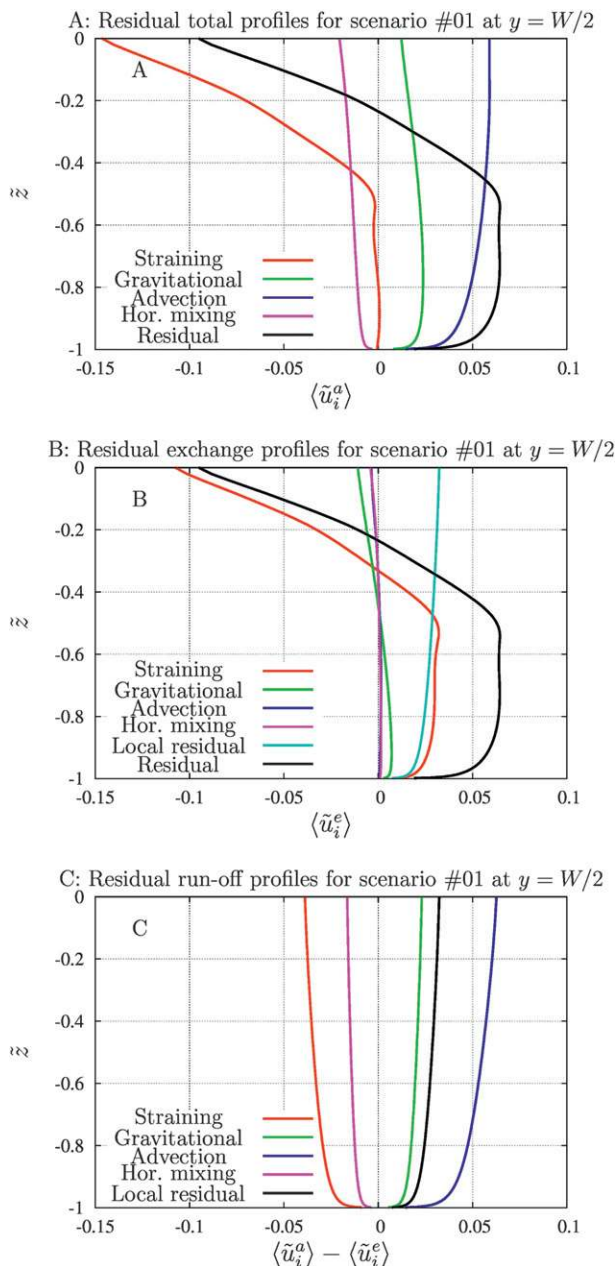

FIG. 7. Residual profiles for the reference scenario 01 at the central location $y = W/2$. (a) Total (exchange + runoff) residual profiles $\langle \tilde{u}_i^a \rangle$ calculated according to the first equation of (11). The black curve is residual profile $\langle \tilde{u} \rangle$. (b) Baroclinic residual profiles $\langle \tilde{u}_i^e \rangle$ calculated according to the first equation of (10). The light blue curve is local residual profile γU_r, and the black curve is residual profile $\langle \tilde{u} \rangle$. (c) Barotropic residual profiles $\langle \tilde{u}_i^a \rangle - \langle \tilde{u}_i^e \rangle$ calculated according to the difference between the first equations of (11) and (10). The black curve is local residual profile γU_r.

may reverse the strain-induced lateral circulation. It seems that the orientation of these circulation cells depends sensitively on the timing of the lateral potential energy releases and the vertical mixing (cf. with Figs.
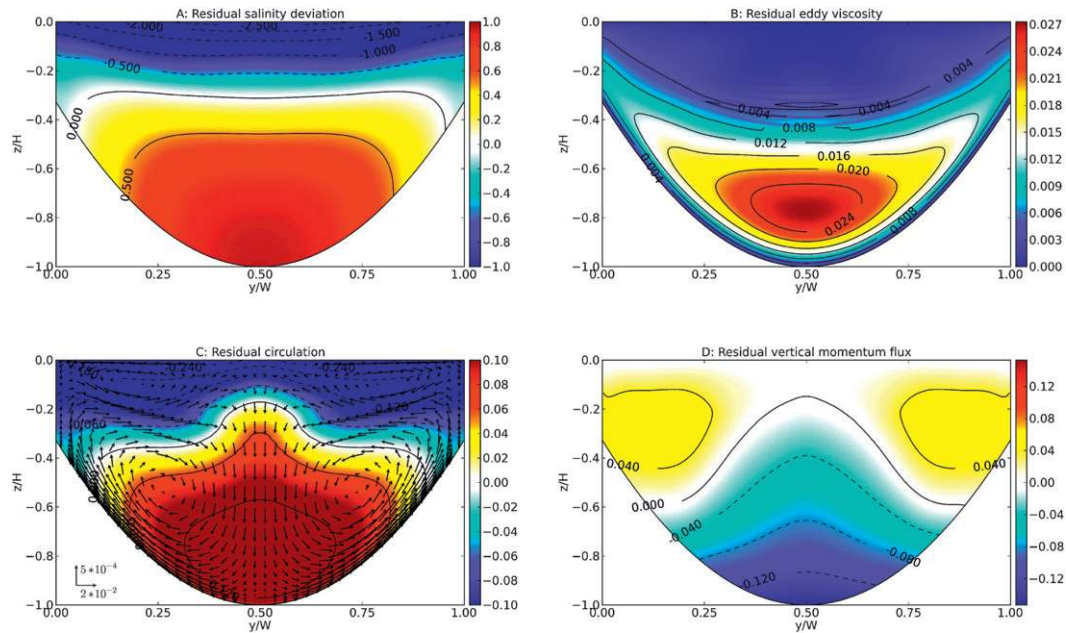
FIG. 8. Scenario 03 (large Si): Nondimensional tidal residual results; see caption in Fig. 5 for details.

4e,f). Both, gravitational and strain-induced lateral circulation support upward residual vertical velocity in the center of the flow. However, this is completely compensated by a strong downward advection-induced vertical velocity and can clearly be seen in all of the following sensitivity studies. This process induces a tendency of the residual vertical velocity to be directed downward in the center of the channel.

b. Sensitivity to Si

The Simpson number Si can easily be modified by changing the longitudinal salinity gradient. Setting the Simpson number to a value of Si = 0.0456 (i.e., taking half of the value of the reference case) results in a strong weakening of the tidal asymmetry, as can be seen in a 50% reduction in residual vertical momentum flux (not shown). Residual circulation is also reduced by about 50% (see Table 2), which is consistent to the finding that the intensity of estuarine circulation scales with Si (see Geyer et al. 2000; Scully et al. 2009; Burchard and Hetland 2010). Also gravitational circulation, advectively driven circulation, and residual runoff circulation are substantially reduced for this low Si case (see Table 2).

The situation profoundly changes when the Simpson number is doubled with respect to the reference scenario: that is, to Si = 0.182 (see Figs. 8–10). This value of Si is at the margin of periodic stratification, and a slight increase would result in runaway stratification, because a longitudinal salinity gradient constant in time and

space is not consistent anymore (see the discussion in section 5). For such high values of Si, Burchard and Hetland (2010) have shown that residual circulation no longer scales proportionally to Si. As a consequence, the residual circulation is now more than doubled compared to the reference case and amounts to a maximum value of $\mathcal{M}(\langle\tilde{u}\rangle) = 0.0972$ (see Fig. 8a), compared to $\mathcal{M}(\langle\tilde{u}\rangle) = 0.0406$ for the reference case. Mixing is strongly reduced in the upper half of the water column (Fig. 8b). Apart from that, the most striking change is the reduction of the straining residual exchange circulation (Fig. 9b) down to a negative contribution of $\mathcal{M}(\langle\tilde{u}_1^e\rangle) = -0.013$ (Table 2, however still with a weak near-bottom up-estuary component; Fig. 9b), whereas gravitational residual exchange circulation (Fig. 9d) and advectively driven residual exchange circulation (Fig. 9f) have increased to values of $\mathcal{M}(\langle\tilde{u}_2^e\rangle) = 0.0544$ and $\mathcal{M}(\langle\tilde{u}_4^e\rangle) = 0.0576$, respectively.

The total contributions to residual circulation from gravitational circulation and advectively driven circulation (Figs. 9c,e) are strongly increased (and only partially compensated by an increased down-estuary contribution from tidal straining and horizontal mixing; Figs. 9a,g) such that now the local runoff circulation in the center of the flow amounts to a vertical-mean value of $U_r(W/2)/U_t > 0.07$ (Fig. 9h).

An explanation for the collapse of the tidal straining circulation in the center of the channel can be found in Fig. 10. In the near-surface region low eddy viscosity (dark blue color in Fig. 10d, indicating negative values of
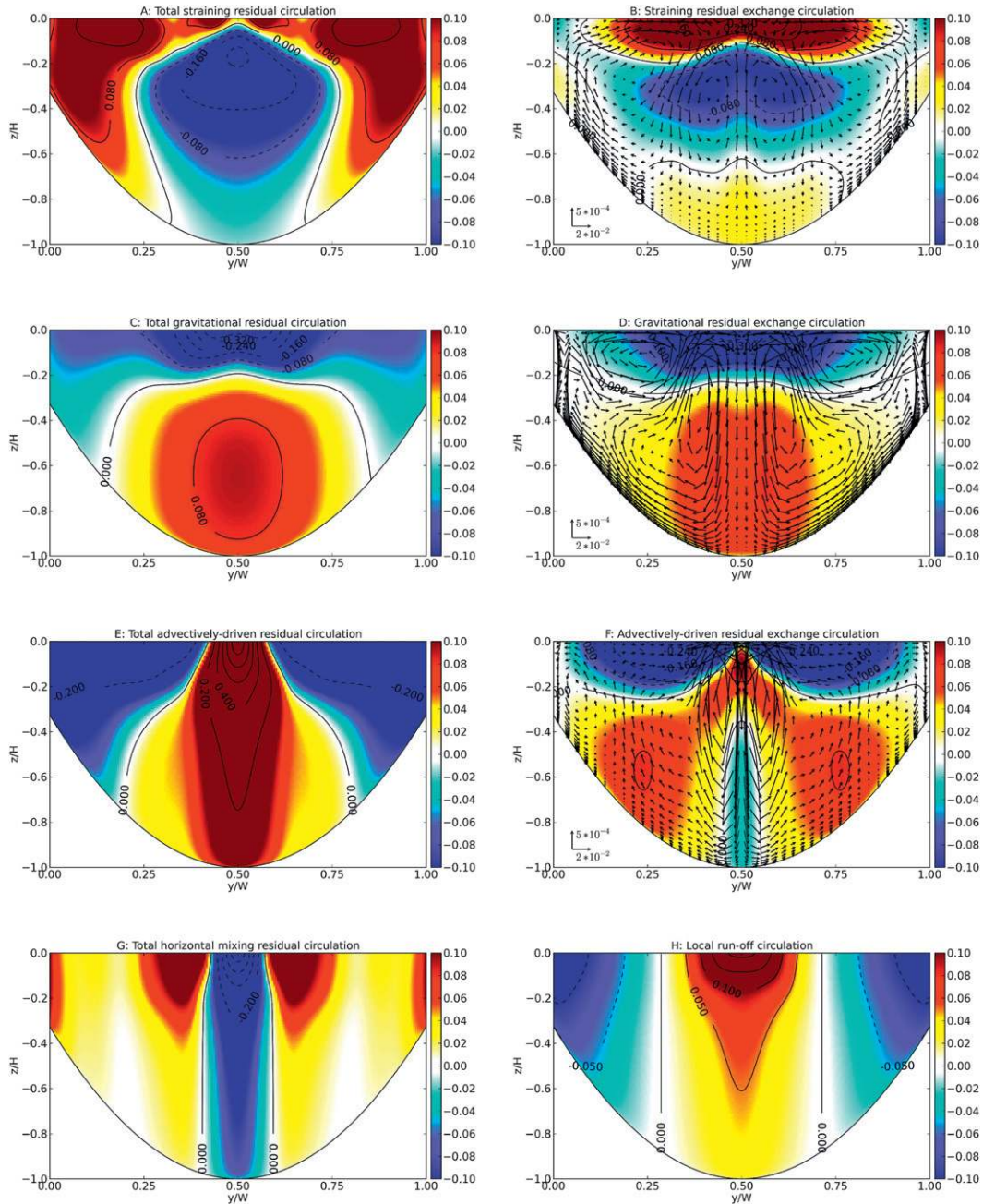
FIG. 9. Scenario 03 (large Si): Nondimensional tidal residual results; see caption in Fig. 6 for details.

A'_v) coincides with negative shear (negative value of $\partial_z u'$), such that $\langle A'_v \partial_z u' \rangle > 0$ in that area, just as in the case of classical straining circulation in the lower half of the water column (see, e.g., Fig. 4). Therefore, the longitudinal straining circulation shows a strong up-estuary component near the surface. Because the shear–viscosity covariance is scaled by the tidal-mean viscosity $\langle A_v(z) \rangle$ [see the term $\mathcal{A}_1$ in (A5)], the contribution of this reverted straining is emphasized in the upper half of the water

column because of the small near-surface eddy viscosity. Only at the sides, the straining residual exchange circulation acts in the classical sense, because there the local Si is smaller because of the reduced local water depth.

The dependence of the longitudinal estuarine circulation and its composition on the Simpson number is shown in Fig. 11a, where Si varies over more than one order of magnitude from Si = 0.01 to Si = 0.2. Between Si = 0.05 and Si = 0.12 estuarine circulation as well its
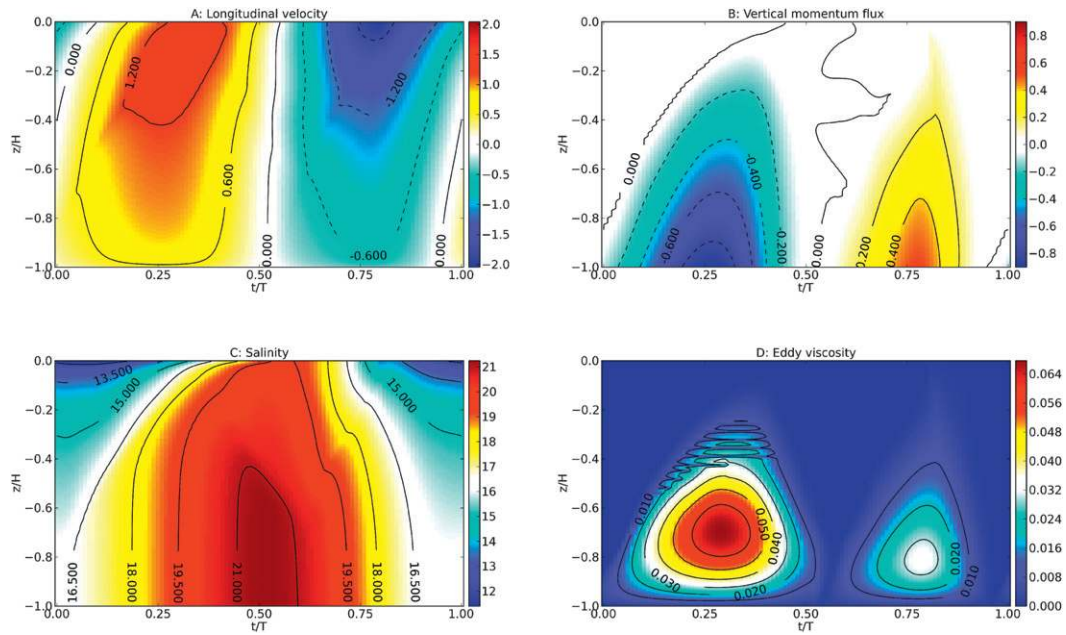
FIG. 10. Scenario 03 (large Si): Time series of profiles of (a) longitudinal velocity, (b) vertical momentum flux, (c) salinity, and (d) eddy viscosity in the center of the channel.

contributors scales about linearly with Si. Gravitational circulation scales linearly with Si even for the entire range Si < 0.12, whereas estuarine circulation and its contributions from tidal straining and lateral advection increase significantly more than linearly with Si for Si < 0.05. For Si > 0.12, the contributions from gravitational circulation and lateral advection increase dramatically to compensate for the increasingly negative contribution from tidal straining. For the whole range Si < 0.12 (i.e., for tidally energetic flows), the relative contribution of the tidal straining circulation to longitudinal estuarine circulation amounts to about two-thirds, with a maximum of 73% for Si = 0.05.

The lateral circulation and its components are weak for Si < 0.05 (Fig. 11c). For even larger values of Si (Si ≈ 0.1), flood-oriented lateral gravitational circulation (up slope near the bed) and ebb-oriented lateral straining circulation (down slope near the bed) compensate each others (see also Figs. 6b,d), such that lateral residual circulation is weak (Fig. 5c). For larger values of Si, the advective contribution increases such that, for these situations with relative strong horizontal density gradients, lateral residual circulation is strongly flood oriented (see also Fig. 8c).

c. Sensitivity to Un

Although, for fixed Si, changes in Un are in reality (and in the model used here) obtained by adjusting the tidal velocity amplitude (e.g., shift between spring and

neap tide) and the longitudinal salinity gradient (variations in river runoff) [see (12)], the effect of changed unsteadiness can most easily be explained by variations in tidal frequency ω. Low tidal frequencies (i.e., relatively long tidal periods) provide more time for the salinity gradient and the currents to interact. Thus, for a smaller value of Un, more pronounced ebb–flood asymmetries would be expected, resulting in stronger estuarine circulation.

By means of a one-dimensional model study, Burchard and Hetland (2010) found a dependence of estuarine circulation on the unsteadiness parameter Un (denoted as inverse Strouhal number in their study), which is proportional to $Un^{-0.2}$. This dependence is reassessed here for the parabolic channel bathymetry by means of varying Un over more than one order of magnitude between Un = 0.009 and Un = 0.14. As clearly seen in Fig. 11b, estuarine circulation depends on the unsteadiness parameter Un (i.e., on the relative tidal frequency). A relatively large value of Un (i.e., a relatively high tidal frequency) implies that the time for the tidal flow to establish tidal asymmetries is relatively short, with the result that the residual circulation intensity is small. For small values of Un (Un < 0.02), the sensitivity of the estuarine circulation and its composition is weak, because they scale with about $Un^{-0.2} \cdots Un^{-0.4}$. This weakly negative but significant scaling is in agreement with the simplified one-dimensional situations studied by Burchard and Hetland (2010). For small values of
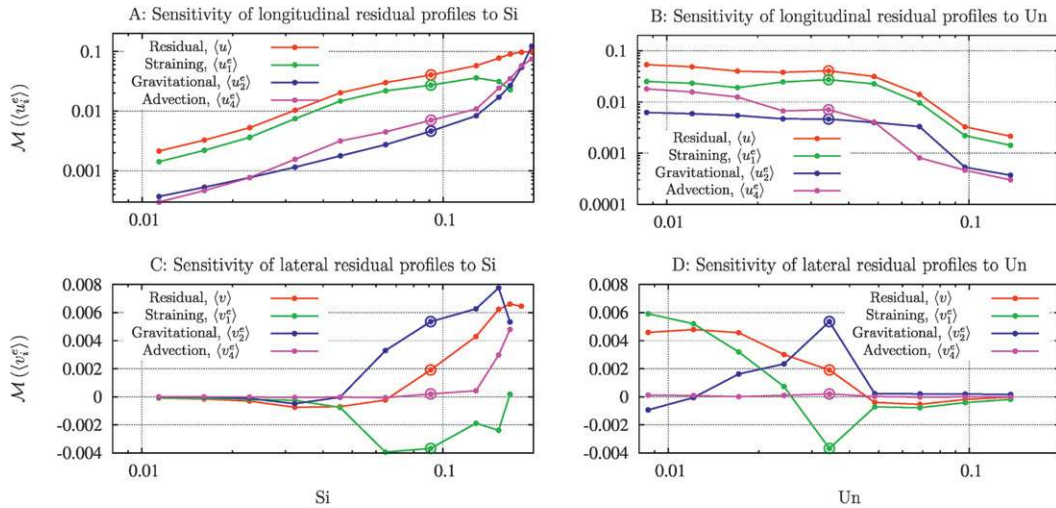
FIG. 11. Sensitivity of (a),(b) longitudinal (logarithmic scale) and (b),(d) lateral (linear scale) residual exchange profiles to (a),(c) the Simpson number Si and (b),(d) the unsteadiness number Un as variation of the reference scenario 01. For the lateral circulation, positive values denote flood-oriented circulation (upslope near the bed). Values for the reference scenario are marked with a circle. For Si > 0.17, the truncation error of the lateral circulation analysis became too large for obtaining significant results.

Un, the advective contribution is comparable to the straining contribution. However, for increasing values of Un, the advection contribution collapses (see also Table 2). This is because it takes quite some time for the lateral circulation to evolve, which is the driver of the advective contribution to longitudinal circulation.

The latter can be clearly seen in Fig. 11d. For Un > 0.04, lateral residual circulation collapses, whereas, for lower values of Un, the lateral residual circulation is mainly resulting from an imbalance between gravitational and straining residual lateral circulation.

d. Variation of z_0^b

Changes in bottom roughness z_0^b primarily have two effects. First, the near-bottom vertical scaling in the water column is changed. Second, the conversion between current velocity scaling by U_t and friction velocity scaling by U_* is changed. Thus, dependence of the estuarine circulation and its composition on relative bed roughness, $z_0^b/\overline{H}$, are expected. An increase of the bed roughness by a factor of 10 in relation to the reference case leads to an increase of estuarine circulation [from $\mathcal{M}(\langle u \rangle) = 0.0406$ to $\mathcal{M}(\langle u \rangle) = 0.0473$] mostly due to an increase in the tidal straining contribution [from $\mathcal{M}(\langle u_1^e \rangle) = 0.0273$ to $\mathcal{M}(\langle u_1^e \rangle) = 0.0341$] (see Table 2). One explanation for this could be that, according to the law of the wall, for unchanged bottom friction velocity and unchanged vertical-mean current velocity, larger values of bottom roughness increase vertical shear outside a narrow boundary layer near the bed. Thus, tidal

currents over rough bottoms are more sensitive to asymmetries in vertical mixing than flows over smooth beds. Indeed, Table 2 shows this by means of a reduced tidal straining of $\mathcal{M}(\langle u_1^e \rangle) = 0.0211$.

e. Variation of width

Table 2 shows a strong impact of estuary width on the intensity of estuarine circulation, mostly on the account of variations in tidal straining circulation. For a narrow estuary ($W = 500$ m), estuarine circulation [$\mathcal{M}(\langle u \rangle) = 0.0278$] and tidal straining [$\mathcal{M}(\langle u_1^e \rangle) = 0.0166$] are strongly reduced in relation to the reference case; for a wide estuary ($W = 2000$ m), both are significantly increased [$\mathcal{M}(\langle u \rangle) = 0.0521$ and $\mathcal{M}(\langle u_1^e \rangle) = 0.0414$]. This effect can be explained as follows (see also Fig. 12): During flood, lateral differential advection of salt is similar for both the narrow and the wide estuary. However, for the narrow estuary, the resulting lateral density gradients are larger by a factor of 4, as compared to the wide estuary. Therefore, a stronger lateral straining is seen during flood for the narrow estuary, resulting in stronger vertical mixing of salt, which (i) slightly reduces eddy viscosity during flood, compared to the wide estuary (Fig. 12), and (ii) reduces the lateral density differences much more than in the wide estuary. Thus, at the end of flood, the maximum bottom-to-surface salinity difference is 0.3 psu for the narrow estuary and 1.0 psu for the wide estuary. For the subsequent ebb in the narrow estuary, ebb mixing wins over ebb straining and reduces this further to less than 0.1 psu, whereas, in the wide estuary, ebb straining wins over
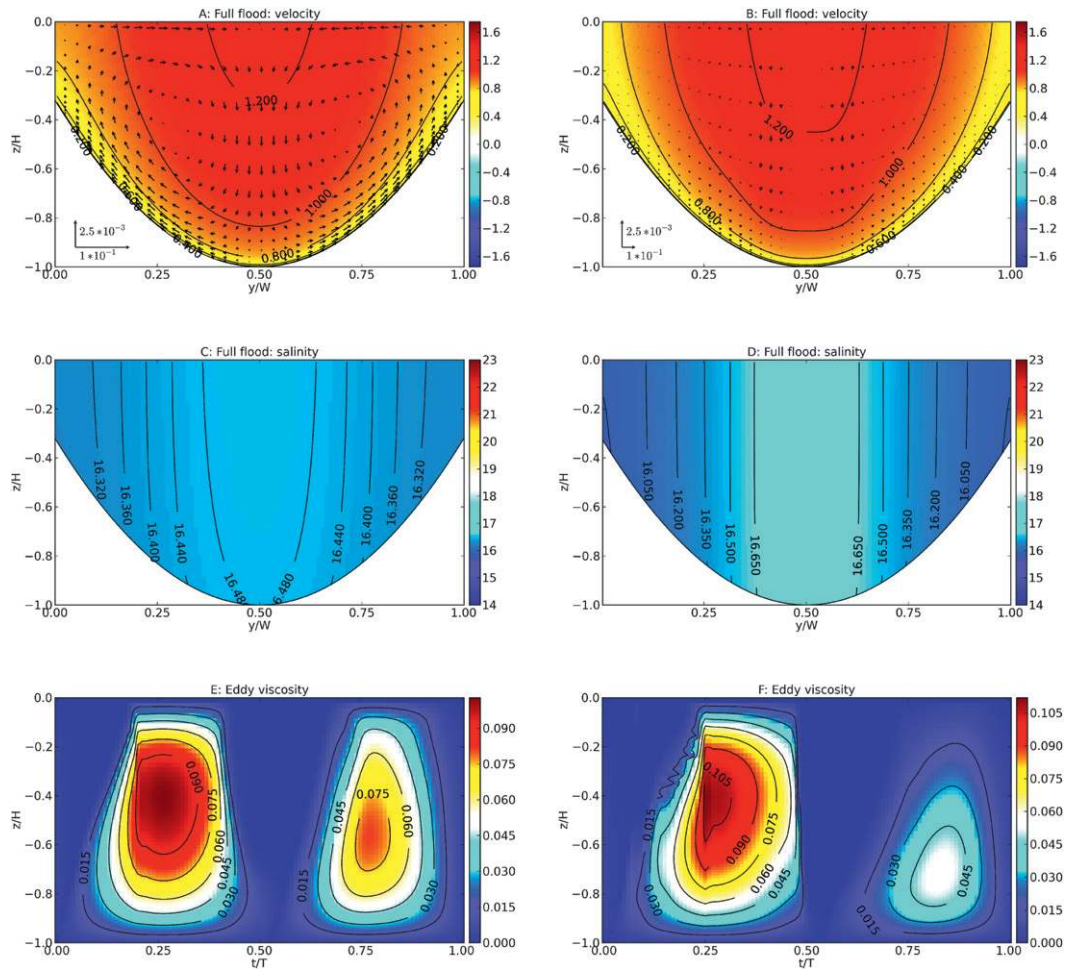
FIG. 12. Comparison of (a),(b) longitudinal velocity and (c),(d) salinity for full flood and (e),(f) eddy viscosity in the central location over a tidal period for scenarios (a),(c),(e) 08 (narrow channel with $W = 500$ m) and (b),(d),(f) 09 (wide channel with $W = 2000$ m).

ebb mixing and increases the bottom-to-surface density gradient to a value of almost 2 psu (not shown). Thus, the different ebb dynamics in the narrow and the wide estuary result in a pronounced mixing asymmetry in the wide estuary (see Fig. 12), leading to the strong tidal straining circulation.

Concerning the influence of estuary width to the other two important processes for generating estuarine circulation, the effect of gravitational circulation is slightly reduced for the narrow estuary (see Table 2) because of increased tidally averaged eddy viscosity (see Fig. 12). In contrast to that, the lateral advection contribution is reduced for the wide estuary, which is in accordance to the arguments by Lerczak and Geyer (2004), who discuss that for wider estuaries the time to significantly move fluid parcels across the estuary becomes longer than the vertical mixing time scale. It should be noted that, for the limit of an infinitely wide estuary, this two-dimensional

case should collapse into the one-dimensional case investigated by Burchard and Hetland (2010), including vanishing contributions from lateral advection. However, for the present case of relatively weak stratification, both contributions are small compared to the tidal straining contribution.

5. Discussion and conclusions

The present study has shed light on a number of processes relevant for longitudinal and lateral estuarine circulation that could not be quantitatively assessed in other studies because of the use of constant viscosity or the assumption of lateral homogeneity. Specifically, the estuarine circulation analysis tool developed by Burchard and Hetland (2010) helped to understand the composition of estuarine circulation in tidally energetic estuaries.

The relevance of the estuarine circulation for tracer transport in coastal areas is obvious. When denoting any tracer concentration by c, then the residual tracer transport is

$$\int_A \langle uc \rangle \, dA = u^0 \int_A \langle c \rangle \, dA + \int_A u^e \langle c \rangle \, dA + \int_A \langle u'c' \rangle \, dA, \tag{17}$$

where the tidal residual flow has been decomposed into a cross-sectional average u^0 and an exchange flow with zero cross-sectional mean u^e. In (17), the first term on the right-hand side is the transport due to the river discharge, the second term is the transport due to estuarine circulation, and the third term is due to the covariance between velocity and concentration (see also Lerczak et al. 2006). For a tidal-mean concentration that is higher in the lower than in the upper half of the water column (e.g., for particulate suspended matter or salt), an up-estuary transport is resulting from the estuarine circulation term, which typically is compensated by the other two terms. During the present study, we found that the volume fluxes (see Table 2) are generally mirrored by the salt fluxes (not shown), although the tidal mean salinity shows a clear spatial structure, specifically in the case of stronger stratification (see Fig. 8).

It could be shown that in channelized estuaries tidal straining is the dominant process for the generation of the longitudinal estuarine circulation for relatively weak stratification (Si $\leq$ 0.15). The value of an approximate ²⁄₃ contribution found by Burchard and Hetland (2010) in a one-dimensional water column study is even exceeded here, most likely because of the additional contribution from lateral advection of longitudinal shear.

For stronger stratification, because it typically occurs in partially mixed estuaries, the contribution from the tidal straining collapses and becomes negative for Si > 0.15. The reasons are found in the near-surface covariance between vertical shear and eddy viscosity (see section 4b). Because the dynamics near the surface strongly depend on surface wind stress, surface heat fluxes, and surface waves, processes which have been ignored here, it is not clear at this point how much stake to put in the exact value of 0.15.

The significant contribution of the lateral advection to longitudinal estuarine circulation, which has been discussed by several authors (e.g., Lerczak and Geyer 2004; Scully et al. 2009), can, for the first time, be quantified here. For a large range of parameters, this advectively driven circulation is comparable in intensity to gravitational circulation, which has been thought until recently to be the dominant process for estuarine circulation. The simulations with strong stratification carried out in the present study

show that gravitational circulation may significantly dominate over the advectively driven contribution, probably because of the suppression of lateral circulation by stable stratification, as suggested by Lerczak and Geyer (2004).

Most major contributors to longitudinal estuarine circulation seem to roughly scale with the Simpson number, as shown in Fig. 11a. The estuarine circulation itself is roughly proportional with Si over the entire parameter range investigated here. For large Si, the gravitational and the advectively driven contributions grow overproportionally with Si to compensate for the collapse of the tidal straining contribution.

As discussed in section 4c, estuarine circulation depends on the unsteadiness parameter Un (i.e., on the relative tidal frequency). A relatively large value of Un (i.e., a relatively high tidal frequency) implies that the time for the tidal flow to establish tidal asymmetries is relatively short, with the result that the residual circulation intensity is small. For smaller values of Un (Un < 0.02), the sensitivity of the estuarine circulation and its composition is weak. This result is in agreement with the simplified one-dimensional model study by Burchard and Hetland (2010).

The advective contribution to longitudinal estuarine circulation is generated by the lateral residual circulation. It can be clearly seen in Fig. 11 that the collapse of lateral circulation due to small Si or large Un leads to a substantial decrease of the advectively driven longitudinal residual exchange circulation.

One further important aspect of estuarine circulation has been found in the present study that has not been discussed previously: tidal straining and thus estuarine circulation is strongly dependent on the width of the estuary. This effect is mainly due to a lateral density gradient forcing, which is increased for narrow estuaries (similar lateral density differences due to similar horizontal differential advection), thus promoting increased vertical mixing and substantial reduction of flood to ebb stratification.

The scientific approach chosen here, using a two-dimensional cross-sectional plane forced with a constant in time and space salinity gradient, has the strong advantage that high numerical resolution can be obtained at reasonable computational cost, thus minimizing discretization errors. Furthermore, the parameter space under consideration is much smaller than for fully three-dimensional numerical experiments. However, these idealizations also have their downside. Multiplication with S and subsequent tidal averaging and area integration of the salinity equation (9) leads, after some analytical transformations, to the following equation for the area-integrated advective salinity flux:

$$\int_A \langle uS \rangle \, dA = \frac{-\int_A \langle K_v (\partial_z S)^2 \rangle \, dA}{\partial_x S}, \qquad (18)$$

which means that the tidally averaged cross-sectionally integrated salt flux is equal to the tidally averaged cross-sectionally integrated salinity variance dissipation, normalized by the longitudinal salinity gradient. A similar result was found by Umlauf and Burchard (2011) for the residual heat flux in the oscillating bottom boundary layer of a basin with sloping bottom and stable background stratification. With (18), a negative salinity gradient $\partial_x S$ (i.e., salinity decreasing in up-estuary direction) results in an up-estuary salinity flux even for down-estuary residual transports. This does not pose a practical problem in the cross-sectional simulations but indicates that, in three-dimensional estuaries correlations of the advective salt flux, the tidal velocity and the salinity with the salinity gradient (which are neglected in the present study because of the choice of a constant longitudinal salinity gradient) are essential.

The use of a constant salinity gradient has the practical implication that, for too large Simpson numbers, periodic solutions are not obtained. This can be demonstrated as follows: Tidal averaging and area integration of the equation [(9)] for the whole cross section above a horizontal line at a position $\hat{z} > -H_{\min}$ leads to

$$\int_0^W \int_{\hat{z}}^0 \langle u \rangle \, dz \, dy = \frac{1}{\partial_x S} \int_0^W (\langle wS \rangle |_{\hat{z}} - \langle K_v \partial_z S \rangle |_{\hat{z}}) \, dy; \qquad (19)$$

that is, the residual flow in the upper layer has to be balanced by advective and turbulent vertical volume fluxes (salt fluxes scaled by the salt gradient). For strong stratification, the left-hand side of (19) is large and negative (down-estuary residual flux near the surface), but, at the same time, vertical volume fluxes are reduced. This can be clearly seen in Fig. 8c, where there is a strong down-estuary residual flux for $z/H > -0.2$. At the same time, vertical mixing is strongly suppressed (Fig. 8b). For much stronger stratification than in scenario 03, the balance given by (19) can no longer hold, indicating that the underlying assumption of a periodic solution is violated.

These limitations discussed above can only be overcome by applying the residual circulation analysis introduced by Burchard and Hetland (2010) for fully three-dimensional estuary models. Because this method requires a high resolution in space to minimize numerical truncation errors and periodic solutions to compute tidal residuals, the investigation of complex bathymetries or strong density gradient forcing is quite demanding on present-day computers. Furthermore, the

inclusion of Stokes drift as a driver for estuarine circulation (which has been switched off in the present study by means of a rigid-lid condition) requires the definition of a relevant time-averaging procedure in a water column with significant depth variations with time.

APPENDIX

Derivation of Residual Circulation Equations

As a first step toward decomposition of the residual circulation, (4) is tidally averaged and then vertically integrated from the vertical coordinate z to the surface at $z = 0$:

$$\langle A_v \partial_z u \rangle = \int_z^0 \int_{\tilde{z}}^0 \langle [\partial_x b] \rangle \, d\overline{z} \, d\tilde{z} - \tau_x^s - \int_z^0 \partial_y \langle uv \rangle \, d\tilde{z} + \langle uw \rangle$$
$$+ \int_z^0 \partial_s \langle A_s \partial_s u \rangle \, d\tilde{z} + f \int_z^0 \langle v \rangle \, d\tilde{z} + z \langle [P^x] \rangle \quad \text{and}$$

$$\qquad (A1a)$$

$$\langle A_v \partial_z v \rangle = \int_z^0 \int_{\tilde{z}}^0 \partial_y \langle b \rangle \, d\overline{z} \, d\tilde{z} - \tau_y^s - \int_z^0 \partial_y \langle vv \rangle \, d\tilde{z} + \langle vw \rangle$$
$$+ \int_z^0 \partial_s \langle A_s \partial_s v \rangle \, d\tilde{z} - f \int_z^0 \langle u \rangle \, d\tilde{z} + z \langle P^y \rangle.$$

$$\qquad (A1b)$$

After decomposition of the eddy viscosity and the longitudinal and lateral velocity components into a tidal mean and a fluctuating part with

$$u = \langle u \rangle + u', \quad \langle u' \rangle = 0, \quad v = \langle v \rangle + v', \quad \langle v' \rangle = 0,$$
$$A_v = \langle A_v \rangle + A_v', \quad \langle A_v' \rangle = 0, \qquad (A2)$$

such that

$$\langle A_v \partial_z u \rangle = \langle A_v \rangle \partial_z \langle u \rangle + \langle A_v' \partial_z u' \rangle \quad \text{and} \quad \text{(A3a)}$$

$$\langle A_v \partial_z v \rangle = \langle A_v \rangle \partial_z \langle v \rangle + \langle A_v' \partial_z v' \rangle, \quad \text{(A3b)}$$

Eq. (A1) is transformed by means of division by $\langle A_v \rangle$ and subsequent vertical integration from the bottom at $z = -H$ to the vertical coordinate z (note that this is the second vertical integration, in correspondence to the double vertical integration carried out for cases with vertically constant eddy viscosity):

$$\langle u \rangle = \sum_{i=1}^{6} \int_{-H}^{z} \mathcal{A}_i \, d\hat{z} + \langle [P^x] \rangle \int_{-H}^{z} \frac{\hat{z}}{\langle A_v \rangle} \, d\hat{z} \quad \text{and} \quad \text{(A4a)}$$

$$\langle v \rangle = \sum_{i=1}^{6} \int_{-H}^{z} \mathcal{B}_i \, d\hat{z} + \langle P^y \rangle \int_{-H}^{z} \frac{\hat{z}}{\langle A_v \rangle} \, d\hat{z}, \quad \text{(A4b)}$$

with

$$\mathcal{A}_1 = \frac{-\langle A_v' \partial_z u' \rangle}{A_v}, \quad \mathcal{A}_2 = \frac{\int_z^0 \int_{\hat{z}}^0 \langle [\partial_x b] \rangle \, d\overline{z} \, d\tilde{z}}{\langle A_v \rangle},$$

$$\mathcal{A}_3 = \frac{-\tau_x^s}{\langle A_v \rangle}, \quad \mathcal{A}_4 = \frac{-\int_z^0 \partial_y \langle uv \rangle \, d\tilde{z} + \langle uw \rangle}{\langle A_v \rangle},$$

$$\mathcal{A}_5 = \frac{\int_z^0 \partial_s \langle A_s \partial_s u \rangle \, d\tilde{z}}{\langle A_v \rangle}, \quad \mathcal{A}_6 = \frac{f \int_z^0 \langle v \rangle \, d\tilde{z}}{\langle A_v \rangle} \quad \text{and} \quad \text{(A5a)}$$

$$\mathcal{B}_1 = \frac{-\langle A_v' \partial_z v' \rangle}{\langle A_v \rangle}, \quad \mathcal{B}_2 = \frac{\int_z^0 \int_{\tilde{z}}^0 \partial_y \langle b \rangle \, d\overline{z} \, d\tilde{z}}{\langle A_v \rangle}, \quad \mathcal{B}_3 = \frac{-\tau_y^s}{\langle A_v \rangle},$$

$$\mathcal{B}_4 = \frac{-\int_z^0 \partial_y \langle vv \rangle \, d\tilde{z} + \langle vw \rangle}{\langle A_v \rangle}, \quad \mathcal{B}_5 = \frac{\int_z^0 \partial_y \langle A_s \partial_s v \rangle \, d\tilde{z}}{\langle A_v \rangle},$$

$$\mathcal{B}_6 = \frac{-f \int_z^0 \langle u \rangle \, d\tilde{z}}{\langle A_v \rangle}. \quad \text{(A5b)}$$

Note that Eqs. (A1)–(A5) are y and z dependent.

In the final step, the pressure gradient terms in (A4) are eliminated by vertically integrating (A4) for each water column, inserting the longitudinal local vertical-mean residual velocity,

$$U_r(y) = \frac{1}{H} \int_{-H}^{0} \langle u \rangle \, dz, \quad \text{with} \quad \int_A U_r(y) \, dA = Q_0, \quad \text{(A6)}$$

and using (8): that is, the fact that the vertically integrated lateral transports are zero. The vertically integrated equations are then solved for $\langle [P^x] \rangle$ and $\langle P^y \rangle$, which are inserted into (A5) to give

$$\langle u \rangle = \sum_{i=1}^{6} \left\{ \int_{-H}^{z} \mathcal{A}_i \, d\hat{z} - \frac{\gamma(y,z)}{H(y)} \int_{-H}^{0} \int_{-H}^{\overline{z}} \mathcal{A}_i \, d\hat{z} \, d\overline{z} \right\}$$

$$+ \gamma(y,z) U_r(y) = \sum_{i=1}^{6} \langle u_i^e \rangle + \gamma(y,z) U_r(y) \quad \text{and}$$

$$\text{(A7a)}$$

$$\langle v \rangle = \sum_{i=1}^{6} \left\{ \int_{-H}^{z} \mathcal{B}_i \, d\hat{z} - \frac{\gamma(y,z)}{H(y)} \int_{-H}^{0} \int_{-H}^{\overline{z}} \mathcal{B}_i \, d\hat{z} \, d\overline{z} \right\}$$

$$= \sum_{i=1}^{6} \langle v_i^e \rangle, \quad \text{(A7b)}$$

with the nondimensional local runoff function

$$\gamma(y,z) = \frac{H \int_{-H}^{z} \frac{\hat{z}}{\langle A_v \rangle} \, d\hat{z}}{\int_{-H}^{0} \int_{-H}^{\overline{z}} \frac{\hat{z}}{\langle A_v \rangle} \, d\hat{z} \, d\overline{z}}. \quad \text{(A8)}$$

Note that area integration of (A7a) gives the tidal average of (7) and that vertical integration of (A7b) gives (8). With (A7), the residual circulation is decomposed into the sum of various residual exchange contributions ($\langle u_i^e \rangle$, $\langle v_i^e \rangle$) and one local runoff profile contribution, $\gamma(y,z) U_r(y)$.

With $\langle v_i^e \rangle$ denoting nondivergent lateral residual velocity profiles due to various processes, vertical velocities consistent with these profiles $\langle w_i^e \rangle$ can be calculated by integrating

$$\partial_y \langle v_i^e \rangle + \partial_z \langle w_i^e \rangle = 0 \quad \text{(A9)}$$

from the bed upward and applying kinematic boundary conditions at the bed,

$$\langle w_i^e(-H) \rangle = -\langle v_i^e(-H) \rangle \partial_y H = 0. \quad \text{(A10)}$$

Instead of vertically integrating the $\langle u \rangle$ equation in (A4a) for each horizontal coordinate y, one could also apply area integration of (A4a) to eliminate $\langle [P^x] \rangle$,

$$\langle u \rangle = \sum_{i=1}^{6} \left\{ \int_{-H}^{z} \mathcal{A}_i \, d\hat{z} - \frac{\beta(y,z)}{A} \int_A \int_{-H}^{\overline{z}} \mathcal{A}_i \, d\hat{z} \, dA \right\} = \sum_{i=1}^{6} \langle u_i^a \rangle, \quad \text{(A11)}$$

with the nondimensional global runoff function

$$\beta(\gamma, z) = \frac{A \int_{-H}^{z} \frac{\hat{z}}{\langle A_v \rangle} d\hat{z}}{\int_{A} \int_{-H}^{\bar{z}} \frac{\hat{z}}{\langle A_v \rangle} d\hat{z} \, dA}. \quad (A12)$$

One serious accuracy issue is given by the structure of the integrands $\mathcal{A}_i$ and $\mathcal{B}_i$, because the value in the denominator is the tidally averaged eddy viscosity $\langle A_v \rangle$, which approaches a minimum value of $\kappa z_0^b \langle u_* \rangle$ at the bed. Because the individual residual circulation profiles $\langle u_i^e \rangle$ and $\langle v_i^e \rangle$ are results of an integration upward from the bottom, small errors in the near-bottom approximations result in large errors over the whole water column. Therefore, the numerator and the denominator (which is always the tidally averaged eddy viscosity profile $\langle A_v \rangle$) of the terms $\mathcal{A}_i$ and $\mathcal{B}_i$ (which are numerically given at the layer interfaces) are first linearly interpolated individually between the interfaces, and then the integrals (ratios of first-order polynomials) are solved analytically. For all numerators of the $\mathcal{A}_i$ and $\mathcal{B}_i$ and also for the $\langle A_v \rangle$, values at the bottom interface at $z = -H$ are needed. Except for the numerators of $\mathcal{A}_i$ and $\mathcal{B}_1$, $\langle A_v' \partial_z u' \rangle$ and $\langle A_v' \partial_z v' \rangle$, respectively, this is a straightforward calculation.

The values of $\langle A_v \rangle$, $\langle A_v' \partial_z u' \rangle$, and $\langle A_v' \partial_z v' \rangle$ at the bottom are calculated according to boundary conditions derived from the law of the wall,

$$\langle A_v \rangle|_{z=-H} = \langle u^* \rangle \kappa z_0^b; \quad \partial_z \langle u \rangle|_{z=-H} = \frac{\langle u_x^* \rangle}{\kappa z_0^b};$$

$$\partial_z \langle v \rangle|_{z=-H} = \frac{\langle u_y^* \rangle}{\kappa z_0^b}, \quad (A13)$$

such that

$$\langle A_v' \partial_z u' \rangle|_{z=-H} = \langle A_v \partial_z u \rangle|_{z=-H} - \langle A_v \rangle|_{z=-H} \partial_z \langle u \rangle|_{z=-H}$$
$$= \langle u^* u_x^* \rangle - \langle u^* \rangle \langle u_x^* \rangle,$$

$$\langle A_v' \partial_z v' \rangle|_{z=-H} = \langle A_v \partial_z v \rangle|_{z=-H} - \langle A_v \rangle|_{z=-H} \partial_z \langle v \rangle|_{z=-H}$$
$$= \langle u^* u_y^* \rangle - \langle u^* \rangle \langle u_y^* \rangle, \quad (A14)$$

with the bed friction velocity

$$u^* = \{(u_x^*)^2 + (u_y^*)^2\}^{1/2}. \quad (A15)$$

It should be noted that the friction velocity u^* is a result of the turbulence closure model and has to be distinguished from the friction velocity scale U_* defined in (3).

REFERENCES

Arneborg, L., V. Fiekas, L. Umlauf, and H. Burchard, 2007: Gravity current dynamics and entrainment—A process study based on observations in the Arkona Basin. *J. Phys. Oceanogr.,* **37,** 2094–2113.

Baumert, H., and G. Radach, 1992: Hysteresis of turbulent kinetic energy in nonrotational tidal flows: A model study. *J. Geophys. Res.,* **97,** 3669–3677.

Blaise, S., and E. Deleersnijder, 2008: A new parameterisation of salinity advection to prevent stratification from running away in a simple estuarine model. *Ocean Sci.,* **4,** 239–246.

Burchard, H., 1999: Recalculation of surface slopes as forcing for numerical water column models of tidal flow. *Appl. Math. Model.,* **23,** 737–755.

——, 2009: Combined effects of wind, tide and horizontal density gradients on stratification in estuaries and coastal seas. *J. Phys. Oceanogr.,* **39,** 2117–2136.

——, and H. Baumert, 1998: The formation of estuarine turbidity maxima due to density effects in the salt wedge: A hydrodynamic process study. *J. Phys. Oceanogr.,* **28,** 309–321.

——, and K. Bolding, 2002: GETM—A general estuarine transport model. European Commission Tech. Rep. EUR 20253 EN, 157 pp.

——, and R. Hofmeister, 2008: A dynamic equation for the potential energy anomaly for analysing mixing and stratification in estuaries and coastal seas. *Estuarine Coastal Shelf Sci.,* **77,** 679–687.

——, and R. D. Hetland, 2010: Quantifying the contributions of tidal straining and gravitational circulation to residual circulation in periodically stratified tidal estuaries. *J. Phys. Oceanogr.,* **40,** 1243–1262.

——, K. Bolding, T. P. Rippeth, A. Stips, J. H. Simpson, and J. Sündermann, 2002: Microstructure of turbulence in the northern North Sea: A comparative study of observations and model simulations. *J. Sea Res.,* **47,** 223–238.

Chatwin, P. C., 1976: Some remarks on the maintenance of the salinity distribution in estuaries. *Estuarine Coastal Shelf Sci.,* **4,** 555–566.

Chen, S.-N., and L. P. Sanford, 2009: Axial wind effects on stratification and longitudinal salt transport in an idealized, partially mixed estuary. *J. Phys. Oceanogr.,* **39,** 1905–1920.

Cheng, P., and A. Valle-Levinson, 2009: Influence of lateral advection on residual currents in microtidal estuaries. *J. Phys. Oceanogr.,* **39,** 3177–3190.

——, R. E. Wilson, R. J. Chant, D. C. Fugate, and R. D. Flood, 2009: Modelling influence of stratification on lateral circulation in a stratified estuary. *J. Phys. Oceanogr.,* **39,** 2324–2337.

Cheng, Y., V. M. Canuto, and A. M. Howard, 2002: An improved model for the turbulent PBL. *J. Atmos. Sci.,* **59,** 1550–1565.

Geyer, W. R., J. H. Trowbridge, and M. M. Bowen, 2000: The dynamics of a partially mixed estuary. *J. Phys. Oceanogr.,* **30,** 2035–2048.

Hansen, D. V., and M. Rattray, 1965: Gravitational circulation in straits and estuaries. *J. Mar. Res.,* **23,** 104–122.

Hofmeister, R., H. Burchard, and J.-M. Beckers, 2010: Non-uniform adaptive vertical grids for 3D numerical ocean models. *Ocean Modell.,* **33,** 70–86.

Huijts, K. M. H., H. M. Schuttelaars, H. E. de Swart, and A. Valle-Levinson, 2006: Lateral entrapment of sediment in tidal estuaries: An idealized model study. *J. Geophys. Res.,* **111,** C12016, doi:10.1029/2006JC003615.

——, ——, ——, and C. T. Friedrichs, 2009: Analytical study of the transverse distribution of along-channel and transverse residual flows in tidal estuaries. *Cont. Shelf Res.,* **29,** 89–100.

Ianniello, J. P., 1977: Tidally induced residual currents in estuaries of constant breadth and depth. *J. Mar. Res.,* **35,** 755–786.

Jay, D. A., and J. D. Musiak, 1994: Particle trapping in estuarine tidal flows. *J. Geophys. Res.,* **99,** 445–461.

Leonard, B. P., 1991: The ULTIMATE conservative difference scheme applied to unsteady one-dimensional advection. *Comput. Methods Appl. Mech. Eng.,* **88,** 17–74.

Lerczak, J. A., and W. R. Geyer, 2004: Modeling the lateral circulation in straight, stratified estuaries. *J. Phys. Oceanogr.,* **34,** 1410–1428.

——, ——, and R. J. Chant, 2006: Mechanisms driving the time-dependent salt flux in a partially stratified estuary. *J. Phys. Oceanogr.,* **36,** 2296–2311.

Li, C., and J. O'Donnell, 2005: The effect of channel length on the residual circulation in tidally dominated channels. *J. Phys. Oceanogr.,* **35,** 1826–1840.

——, A. Valle-Levinson, K. C. Wong, and K. M. M. Lwiza, 1998: Separating baroclinic flow from tidally induced flow in estuaries. *J. Geophys. Res.,* **103,** 10 405–10 417.

MacCready, P., 2004: Toward a unified theory of tidally-averaged estuarine salinity structure. *Estuaries,* **27,** 561–570.

McGregor, R. C., 1972: The influence of eddy viscosity on the vertical distribution of velocity in the tidal estuary. *Geophys. J. Roy. Astron. Soc.,* **29,** 103–108.

Monismith, S. G., J. R. Burau, and M. Stacey, 1996: Stratification dynamics and gravitational circulation in northern San Francisco Bay. *San Francisco Bay: The Ecosystem,* J. T. Hollibaugh, Ed., American Association for the Advancement of Science, 123–153.

Nunes, R. A., and J. H. Simpson, 1985: Axial convergence in a well-mixed estuary. *Estuarine Coastal Shelf Sci.,* **20,** 637–649.

Pietrzak, J., 1998: The use of TVD limiters for forward-in-time upstream-biased advection schemes in ocean modeling. *Mon. Wea. Rev.,* **126,** 812–830.

Pritchard, D. W., 1952: Salinity distribution and circulation in the Chesapeake Bay estuarine system. *J. Mar. Res.,* **11,** 106–123.

——, 1954: A study of the salt balance in a coastal plain estuary. *J. Mar. Res.,* **13,** 133–144.

——, 1956: The dynamic structure of a coastal plane estuary. *J. Mar. Res.,* **15,** 33–42.

Ralston, D. A., W. R. Geyer, and J. A. Lerczak, 2008: Subtidal salinity and velocity in the Hudson River estuary: Observations and modeling. *J. Phys. Oceanogr.,* **38,** 753–770.

Scully, M. E., W. R. Geyer, and J. A. Lerczak, 2009: The influence of lateral advection on the residual estuarine circulation: A numerical modeling study of the Hudson River estuary. *J. Phys. Oceanogr.,* **39,** 107–124.

Simpson, J. H., J. Brown, J. Matthews, and G. Allen, 1990: Tidal straining, density currents, and stirring in the control of estuarine stratification. *Estuaries,* **26,** 1579–1590.

——, H. Burchard, N. R. Fisher, and T. P. Rippeth, 2002: The semidiurnal cycle of dissipation in a ROFI: Model-measurement comparisons. *Cont. Shelf Res.,* **22,** 1615–1628.

Stacey, M. T., J. R. Burau, and S. G. Monismith, 2001: Creation of residual flows in a partially stratified estuary. *J. Geophys. Res.,* **106,** 17 013–17 037.

——, J. P. Fram, and F. K. Chow, 2008: Role of tidally periodic density stratification in the creation of estuarine subtidal circulation. *J. Geophys. Res.,* **113,** C08016, doi:10.1029/2007JC004581.

Stips, A., H. Burchard, K. Bolding, and W. Eifler, 2002: Modelling of convective turbulence with a two-equation k-ε turbulence closure scheme. *Ocean Dyn.,* **52,** 153–168.

Umlauf, L., and H. Burchard, 2005: Second-order turbulence models for geophysical boundary layers. A review of recent work. *Cont. Shelf Res.,* **25,** 795–827.

——, and ——, 2011: Diapycnal transport and mixing efficiency in stratified boundary layers near sloping topography. *J. Phys. Oceanogr.,* **41,** 329–345.

——, L. Arneborg, R. Hofmeister, and H. Burchard, 2010: Entrainment in shallow rotating gravity currents: A modeling study. *J. Phys. Oceanogr.,* **40,** 1819–1834.

van Aken, H. M., 1986: The onset of stratification in shelf seas due to differential advection in the presence of a salinity gradient. *Cont. Shelf Res.,* **5,** 475–485.

Wong, K.-C., 1994: On the nature of transverse variability in a coastal plain estuary. *J. Geophys. Res.,* **99,** 14 209–14 222.